Charged bosons in a doped Mott insulator: Electronic properties of domain-wall solitons and meron vortices

Mona Berciu and Sajeev John
Department of Physics, University of Toronto, 60 St. George Street, Toronto, Ontario, Canada M5S 1A7
(Received 11 April 1997)

We demonstrate from first principles that when a charge carrier is added to a spin-1/2 antiferromagnetic Mott insulator in either a one- or two-dimensional lattice, the self-consistent, Hartree-Fock ground state consists of a magnetic soliton texture with a doubly degenerate electronic level at the center of the Mott-Hubbard charge gap. This model is appropriate to systems with weak interchain or interlayer magnetic couplings in which long-range antiferromagnetic order is observed in the absence of charge carriers (doping). These magnetic solitons mediate the destruction of the magnetic order as the charge carrier concentration is increased. In a one-dimensional lattice with nearest-neighbor hopping t, on-site Coulomb repulsion U, and self-consistent, antiferromagnetic moment amplitude S, we find that a charged, *fermionic*, magnetic domain wall soliton with a weakly ferromagnetic core, centered between two sites, has lower Hartree-Fock energy than a corresponding charged quasiparticle in one of the Mott-Hubbard bands. However, for $US/t>2$, this soliton is unstable to the formation of a lower energy charged, *bosonic* domain wall soliton, centered on a single site. For $US/t< 2$, both of the above solitons are charged bosons. The self-consistent structure of these solitons exhibits no rotation of the local magnetic moments, but only a local suppression of the local moment amplitude in the vicinity of the hole. In the absence of doping, charge neutral domain wall solitons exhibit spin rotation within their core region. The equilibrium core size ρ is determined by the degree of magnetic anisotropy. The ferromagnetic core soliton exhibits a pair of nondegenerate near-midgap electronic states. The antiferromagnetic core soliton exhibits a pair of nondegenerate electronic states that are symmetric about the midgap energy and that merge into the continuum as the anisotropy effects are made small and the soliton core radius ρ becomes very large. The two-dimensional antiferromagnetic Mott insulator exhibits analogous behavior to the one-dimensional model. This analogy is precise for a 2D antiferromagnet exhibiting *spin flux*. For the undoped Mott insulator, the ferromagnetic core meron vortex (''lotus flower'' configuration of local magnetic moments) exhibits a doubly degenerate electronic midgap state in the continuum model and is the analog of the 1D neutral domain wall soliton. We demonstrate that a hole added to the 2D system can form a charged bosonic collective excitation, in which the spin background around the hole forms a *planar vortex* with local antiferromagnetic correlations at infinity and vanishing local-moment amplitude at the core of the soliton. [S0163-1829(98)01015-7]

I. INTRODUCTION

The occurrence of the high-T_c superconductivity[1] in layered perovskite materials has sparked broad interest[2] in the quantum properties of magnetically correlated electron systems. At low temperature all parent compounds exhibit an antiferromagnetic Mott-Hubbard charge gap.[3] As charge carriers are introduced by doping, this long-range antiferromagnetic (AFM) order disappears, leading to a metallic phase with striking non-Fermi-liquid properties.[4,5] Superconductivity emerges from this unconventional metal as the system is cooled. The development of a microscopic model of this unconventional metal is one of the outstanding issues in quantum many-body theory.[6]

The magnetic behavior of underdoped high-T_c superconductors is consistent with strong antiferromagnetic Heisenberg exchange within the CuO_2 planes and weak anisotropy, which favors in-plane AFM order. Long-range AFM order at finite temperature is sustained by an interplane Heisenberg exchange $J_\perp$, which is 2–5 orders of magnitude weaker than the intraplane exchange interaction J. However, semiclassical spin-wave theory[7] is insufficient in describing this system when it is doped with charge carriers. Within spin-wave theory, the in-plane AFM correlation length ξ diverges exponentially $\xi/a\sim\exp(J/k_BT)$ as the temperature is lowered in the purely two-dimensional (2D) system. 3D magnetic order occurs at a Néel temperature $k_BT_N\sim J_\perp(\xi/a)^2$, where a is the 2D lattice constant. This, however, is inconsistent with the observed insensitivity of T_N to changes in the interplane coupling.[8,9] Substitution of ions that decrease the interplane coupling or changes in the interplane spacing itself lead to a negligible change in T_N. This suggests that T_N is driven largely by a 2D effect. Indeed, in the presence of a small XY anisotropy, ΔJ, of the in-plane exchange interaction, it is plausible that the 2D correlation length ξ diverges at a finite Kosterlitz-Thouless[10] transition temperature $T_{KT}>0$. In this case, an infinitesimal $J_\perp$ between planes could drive a transition to a 3D ordered AFM at a temperature T_N only slightly larger than T_{KT}. The observed insensitivity of T_N to $J_\perp$ is then quite natural.

Another surprising experimental feature of high-T_c superconductors is that hole doping is much more detrimental to the long-range AFM order than substitution of Cu^{2+} by nonmagnetic ions such as Zn^{2+}. The reduction of the Néel temperature with doping is accompanied by a reduction of the local magnetization amplitude, or a magnetic twist near the holes. The measurements show that there is a large local modification of the magnetic properties near the localized holes, and that up to 100 Cu sites are affected by the presence of a single hole.[8]

 © 1998 The American Physical Society

Our hypothesis is that upon doping, charge carriers are cloaked by mobile magnetic vortex solitons with electronic energy levels near the center of the Mott-Hubbard charge-transfer gap. This is analogous to the behavior of the one-dimensional compound polyacetylene, with doping. In both polyacetylene and high-T_c superconductors, doping is accompanied by the emergence of a midinfrared absorption band in the optical conductivity.[11,12]

In this paper we show that the scenario described above, and the detailed analogy with polyacetylene, can be precisely realized using a recently introduced[13] variant of the AFM ground state of the undoped material. We refer to this variant as the *spin-flux* state of the AFM. This state differs from the standard spin-density-wave (SDW) description of the AFM only in that the one-electron wave functions which constitute the spin-flux SDW exhibit a 2π rotation of the internal coordinate frame of the electron (described by three Euler angles) as the electron encircles any elementary plaquette of the two-dimensional lattice. It was shown[14] that in the presence of the *spin flux*, the ground-state energy of the mean-field AFM is lower than in the absence of the spin flux, for a large range of doping concentration and on-site Coulomb repulsion strength U. In our view, quantized spin flux is a new quantum degree of freedom for a many-electron system, corresponding to a hidden ''law of nature.'' This law of nature is hidden in models, such as the Hubbard model, that neglect the finite range of the screened Coulomb interaction between the electrons. However, by including nearest-neighbor Coulomb repulsion effects, it is possible for internal electric fields in the many-electron system to promote internal spin rotation of an electron as it encircles a closed path. It was shown previously[13] that dynamical generation of spin flux in this manner is accompanied by the nucleation of a pair of magnetic skyrmion structures in the AFM background. The presence of these spin-flux-carrying skyrmions leads to a lowering of the average local magnetic moment amplitude S, thereby lowering the overall many-electron energy relative to the conventional Néel state.

In a recent paper[15] we suggested that when charge carriers are added to the antiferromagnet described above, new types of magnetic solitons textures appear, which lead to further disordering of the magnetic background. While it is energetically favorable for a single charge carrier to nucleate a *non-spin-flux-carrying* skyrmion (conventional spin polaron) and thereby occupy a state deep into the Mott-Hubbard charge-transfer gap, in the presence of many charge carriers it is entropically favorable for such spin polarons to dissociate into pairs of merons (vortexlike solitons). This in turn may lead to the quantum analog of a Kosterlitz-Thouless transition[10] characteristic of 2D systems. As the charge carrier concentration increases, the Kosterlitz-Thouless transition temperature T_{KT} rapidly decreases, eventually driving the Néel temperature T_N to zero.

Above the transition temperature T_{KT}, the merons should dictate the behavior of the system. Using a simple continuum model we showed[15] that the ferromagnetic-core merons have a doubly degenerate localized level at the midgap of the Mott-Hubbard gap. This is consistent with the emergence of a broad midinfrared optical absorption band with doping, indicating the existence of electronic levels deep within the gap. Furthermore, since the merons are mobile and the hole is localized in their core, they contribute to the charge transport. Our study indicates that these charged merons are bosons. As such, it is natural to expect non-Fermi-liquid behavior from such charge carriers in the normal phase of high-T_c superconductors for temperatures $T>T_c$.

In addition to a quantum plasma phase of meron vortices, at special charge carrier concentrations merons may form ordered arrays such as stripes and domain wall lines.[16] These states may suppress superconductivity at specific doping fractions.[17] It has been noted earlier that in models that completely neglect the long-range part of the electron-electron Coulomb repulsion, there is a a tendency for charge carriers in an antiferromagnet to phase separate.[18] The incorporation of realistic Coulomb interactions, however, tends to frustrate such phase separation. In our model, nearest-neighbor Coulomb repulsion plays a crucial role in the generation of spin flux and the subsequent stabilization of meron-vortex solitons. In this sense our model provides a specific, microscopic mechanism for the frustration of phase separation, which in turn may be central to the emergence of superconductivity.[18]

We begin with a detailed study of the one-dimensional analogs of the two-dimensional merons. These are domain walls on an AFM chain. We show, using a simple continuum approximation, that the corresponding 1D domain walls and 2D merons have similar electronic spectra. The advantage of the one-dimensional study is that it is much more simple to perform self-consistent calculations on the lattice. Moreover, the 1D results may be directly relevant for the 3D high-T_c superconductors. High-T_c cuprates such as $YBa_2Cu_3O_7$ and its close relatives have quasi-one-dimensional CuO chain structures. Unlike other classic one-dimensional quantum spin chains,[19] which exhibit 3D AFM order at temperatures on the order of 1 K, the CuO chains reveal AFM ordering at temperatures $T_{N_2}\sim 10$–80 K. Experiments measuring the dc resistivity,[20] the infrared and optical conductivity,[21] and the penetration depth in untwinned crystals[22] and ceramics[23] have revealed large anisotropies between the a direction (perpendicular to chains) and the b direction (parallel to chains). These results suggest that substantial currents are carried along the chains in both the normal and superconducting states. The source of superconducting condensate on the chains has not yet been elucidated. On the other hand, it is known[24] that in $RBa_2Cu_3O_{6+x}$ compounds (R=rare earth) at low temperatures ($T<T_{N_2}$), there is a magnetic state in which not only the planes, but also the chains, have AFM order, with large ordered magnetic moments. It is possible that pairs of 1D charged domain walls are relevant to superconductivity on these chains.

Consider a strongly interacting quasi-two-dimensional electron gas described by the tight-binding Hamiltonian,

$$\mathcal{H}=-\sum_{\substack{\langle ij\rangle\\ \sigma}} t_{ij}(a_{i\sigma}^{+}a_{j\sigma}+\mathrm{H.c.})+\sum_{ij} V_{ij}n_in_j, \qquad (1.1)$$

where $a_{i\sigma}^{+}$ creates an electron at site i with spin σ, t_{ij} is the hopping amplitudes from site j to site i on the square lattice,

$\hat{n}_i \equiv \Sigma_{\sigma=1}^{2} a_{i\sigma}^{+} a_{i\sigma}$, and V_{ij} is the Coulomb interaction. For nearest-neighbor hopping ($t_{ij}=t_0$) and purely on-site Coulomb repulsion ($V_{ii}\equiv U$), this reduces to the Hubbard model. In order to capture the effects of spin rotation during the process of electron hopping, we retain the *nearest-neighbor* Coulomb repulsion ($V_{ij}=V$). It is convenient to define the bilinear combination of electron operators $\Lambda_{ij}^{\mu} \equiv a_{i\alpha}^{+} \sigma_{\alpha\beta}^{\mu} a_{j\beta}$, $\mu=0,1,2,3$, for $i \neq j$, as well as the on-site operators $\hat{\vec{S}}_i = 1/2 a_{i\alpha}^{+} \vec{\sigma}_{\alpha\beta} a_{i\beta}$ and $\hat{Q}_i = \hat{n}_i = a_{i\alpha}^{+} \sigma_{\alpha\beta}^{0} a_{i\beta}$. Here σ^0 is the 2×2 identity matrix and $\vec{\sigma} \equiv (\sigma^1, \sigma^2, \sigma^3)$ are the usual Pauli spin matrices. The quantum expectation value $\langle\ \rangle$ of the $\hat{\vec{S}}_i$ and $\hat{Q}_i$ operators in mean-field theory signifies the presence of spin- and charge-density, while those of the Λ_{ij}^{μ} operators are associated with charge currents ($\mu=0$) and spin current ($\mu=1,2,3$). In the spin-flux model,[13,14] we adopt the ansatz that there is no charge current in the ground state $\Lambda_{ij}^{0}=0$ but circulating spin currents exist and take the form $\Lambda_{ij}^{a} = (2t_0/V)\, i\Delta_{ij} \hat{n}_a$, $a=1,2,3$, where $|\Delta_{ij}| = \Delta$ for all i and j, and $\hat{n}$ is a unit vector. In order to keep this article self-contained, we briefly recapitulate the derivation of the spin flux from the above mean-field considerations.

Using the Pauli spin-matrix identity, $\frac{1}{2}\sigma_{\alpha\beta}^{\mu}(\sigma_{\alpha'\beta'}^{\mu})^{*} = \delta_{\alpha\alpha'}\delta_{\beta\beta'}$, it is possible to rewrite the electron-electron interaction terms as follows: $n_i n_j = 2n_i - \frac{1}{2}\Lambda_{ij}^{\mu}(\Lambda_{ij}^{\mu})^{+}$ if $i \neq j$, and $n_{i\uparrow} n_{i\downarrow} = n_i - (\hat{\vec{S}}_i \hat{\vec{S}}_i + \frac{1}{4}\hat{Q}_i \hat{Q}_i)$. Using the Hartree-Fock factorization, $\Lambda_{ij}^{\mu}(\Lambda_{ij}^{\mu})^{+} \rightarrow \langle \Lambda_{ij}^{\mu} \rangle (\Lambda_{ij}^{\mu})^{+} + \Lambda_{ij}^{\mu} \langle \Lambda_{ij}^{\mu} \rangle^{*} + \langle \Lambda_{ij}^{\mu}(\Lambda_{ij}^{\mu})^{+} \rangle - 2\langle \Lambda_{ij}^{\mu} \rangle \langle \Lambda_{ij}^{\mu} \rangle^{*}$, we obtain the mean-field Hamiltonian,

$$\mathcal{H}^{\mathrm{MF}} = -t \sum_{\langle ij \rangle} a_{i\alpha}^{+} T_{\alpha\beta}^{ij} a_{j\beta} + \mathrm{H.c.} + U \sum_i n_{i\uparrow} n_{i\downarrow}. \quad (1.2)$$

Here, $T_{\alpha\beta}^{ij} \equiv (\delta_{\alpha\beta} + i\Delta_{ij}\hat{n}\cdot\vec{\sigma}_{\alpha\beta})/\sqrt{1+\Delta^2}$ are spin-dependent $SU(2)$ hopping matrix elements defined by the mean-field theory, and $t = t_o\sqrt{1+\Delta^2}$. In deriving Eq. (1.2) we have dropped constant terms that simply change the zero of energy in Eq. (1.1) as well as terms proportional to $\Sigma_i n_i$ that simply change the chemical potential.

The on-site interaction term can be rewritten in the (exact) form

$$U \sum_i n_{i\uparrow} n_{i\downarrow} = -U \sum_i \hat{\vec{S}}_i \cdot \hat{\vec{S}}_i - \frac{U}{4} \sum_i \hat{Q}_i \hat{Q}_i + U \sum_i \hat{n}_i. \quad (1.3)$$

The approximation for this term is obtained by making the usual mean-field factorizations keeping the expectation values of the fluctuation terms. These fluctuation terms will play an important role in the self-consistent magnetic soliton energies in the 1D model. We write

$$\hat{\vec{S}}_i \cdot \hat{\vec{S}}_i = 2\hat{\vec{S}}_i \cdot \langle \hat{\vec{S}}_i \rangle + \langle \hat{\vec{S}}_i^2 \rangle - 2\langle \hat{\vec{S}}_i \rangle^2$$

and

$$\hat{Q}_i \hat{Q}_i = 2\hat{Q}_i \langle \hat{Q}_i \rangle + \langle \hat{Q}_i^2 \rangle - 2\langle \hat{Q}_i \rangle^2.$$

Finally, denoting the expectation value of the spin at the site i by $\vec{S}_i = \langle \hat{\vec{S}}_i \rangle$ and the number of electrons (density of charge) by $Q_i = n_i = \langle \hat{Q}_i \rangle$, we obtain the mean-field Hubbard Hamiltonian,

$$\mathcal{H} = \mathcal{H}_{\mathrm{el}} + \mathcal{H}_{\mathrm{const}},$$

where

$$\mathcal{H}_{\mathrm{el}} = -t \sum_{\langle ij \rangle, \alpha\beta} (a_{i,\alpha}^{\dagger} T_{\alpha\beta}^{ij} a_{j,\beta} + \mathrm{H.c.}) - U \sum_{i,\alpha,\beta} a_{i,\alpha}^{\dagger} (\vec{S}_i \cdot \vec{\sigma}_{\alpha,\beta}) a_{i,\beta} + \frac{U}{2} \sum_{i,\alpha} (1 - Q_i) a_{i,\alpha}^{\dagger} a_{i,\alpha} \quad (1.4)$$

and

$$\mathcal{H}_{\mathrm{const}} = U \sum_i (\vec{S}_i^2 + \tfrac{3}{4} Q_i^2 - \tfrac{1}{2} Q_i), \quad (1.5)$$

where $\vec{S}_i = \frac{1}{2}\langle \hat{a}_{i,\alpha}^{\dagger} \vec{\sigma}_{\alpha\beta} \hat{a}_{i,\beta} \rangle$ and $Q_i = \langle \hat{a}_{i,\alpha}^{\dagger} \hat{a}_{i,\alpha} \rangle$ must be calculated self-consistently.

It was shown previously[14] that the ground state energy depends on the rotation matrices T^{ij} only through the plaquette matrix product $T^{12}T^{23}T^{34}T^{41} \equiv \exp(i\hat{n}\cdot\vec{\sigma}\Phi)$. Here, Φ is the spin flux that passes through each plaquette and 2Φ is the angle through which the internal coordinate system of the electron rotates as it encircles the plaquette.

We use the ansatz that a spin flux of $\Phi = \pi$ penetrates each plaquette, i.e., $T^{12}T^{23}T^{34}T^{41} = -1$ around each plaquette. This means that the one-electron wave functions are forced to be antisymmetric around *each* of the elementary plaquettes of the square lattice. This uniform spin-flux phase may be regarded as an alternative mean-field ground state of the Hubbard model, which describes spin-dependent scattering and the resulting many-body correlations.

We emphasize, however, that this mean field is a ''false ground state''[25] at finite doping, analogous to the ''false vacuum'' in early models of quantum chromodynamics.[26] In the presence of charge carriers this mean field is unstable to the proliferation of topological fluctuations (magnetic solitons), which eventually destroy the LRO. In this sense, our model goes beyond simple mean-field theory.

We begin by presenting the self-consistent results for the 1D lattice model using the above mean-field factorization for the on-site interaction term. These results are recaptured using a simple continuum approximation. We show that this continuum model can be mapped onto the corresponding continuum model of domain walls in polyacetylene.[27] From an energetic point of view, isolated domain walls in a quasi-one-dimensional magnet and single vortices in a quasi-two-dimesional magnet have linearly and logarithmically divergent creation energies, respectively. Consequently, these solitons must be created in pairs in a real system.

Our study of the 2D spin-flux model demonstrates a striking correspondence between the spectra of the domain wall solitons and polarons of the 1D system, with merons and skyrmions, respectively, of the 2D system. This analogy is facilitated by the relativistic one-electron dispersion relations of the 2D spin-flux model. These calculations lend support to

a physical picture of the 2D CuO planes in which skyrmion fluctuations reduce the magnitude of the ordered local AFM magnetic moment at low doping. With increased doping, the charged spin polarons may lower their energy by forming bound meron-antimeron pairs. With further doping, these meron pairs dissociate through a Kosterlitz-Thouless transition into a quantum liquid of free merons,[28] which destroy the long-range order. The time scale for electronic excitations across the Mott-Hubbard charge gap is very small compared to the time scale of magnetic fluctuations so that a well-defined, instantaneous Mott-Hubbard gap structure exists even within the spin-liquid phase.

The charged merons are mobile planar vortex configurations of the spin background. We demonstrate that they are spinless bosons. Charge transport mediated by bosonic meron vortices exhibits highly non-Fermi-liquid behavior and non-Drude behavior in the low-frequency conductivity. Also, the midgap states of such carriers are consistent with the appearance of the broad midinfrared band upon doping.

II. QUASI-ONE-DIMENSIONAL AFM CHAIN

For intuition purposes, we first consider the electronic structure of topological defects in a 1D antiferromagnet with long-range order (LRO). This LRO is induced by the magnetic interaction of electrons in the chain with other electrons in the 3D crystal in which the chain is embedded.

The Hamiltonian of the 1D chain with nearest-neighbor hopping contains no nontrivial closed loops through which spin flux can penetrate. Therefore, we set $T^{ij}=1$ in this model. For a half-filled chain, we set $Q_i=1$, since we do not consider charge-density-wave states.

Our model 1D Hamiltonian becomes

$$\mathcal{H}_{\rm mf}=-t\sum_{i,\sigma}(\hat{a}^{\dagger}_{i,\sigma}\hat{a}_{i+1,\sigma}+\hat{a}^{\dagger}_{i+1,\sigma}\hat{a}_{i,\sigma}) - U\sum_{i,\alpha,\beta}\hat{a}^{\dagger}_{i,\alpha}(\vec{S}_i\cdot\vec{\sigma}_{\alpha,\beta})\hat{a}_{i,\beta}+U\sum_i(\vec{S}_i^2+1/4), \tag{2.1}$$

where $\vec{S}_i=(-1)^{(i+1)}S\vec{e}_z$ and $\vec{e}_z$ is a unit vector of some arbitrary direction. The value of S is determined self-consistently.

The electronic part of the undoped AFM mean-field Hamiltonian consists of two electronic bands characterized by the dispersion relations

$$E_k^{c/v}=\pm\sqrt{\epsilon_k^2+(US)^2},\quad k\in(-\pi/2a,\pi/2a],$$

where $\epsilon_k=-2t\cos(ka)$ and a is the lattice constant.

Each of these levels is doubly degenerate, corresponding to spin ''up'' and spin ''down'' degrees of freedom: if the wave function corresponding to spin up is concentrated mainly at the odd sites, then the degenerate wave function corresponding to spin down is concentrated mainly at the even sites, and vice versa (see Appendix A). At half-filling, all the states in the valence band ($E_k^v<0$) are occupied, while all the states in the conduction band ($E_k^c>0$) are empty. The two bands are separated by a Mott-Hubbard charge gap of magnitude $2US$.

TABLE I. Number of states per site, per spin direction, in the valence and conduction bands.

# states	n=even $\sigma=\uparrow$	n=even $\sigma=\downarrow$	n=odd $\sigma=\uparrow$	n=odd $\sigma=\downarrow$
$\int_{\rm c\ band}dE\rho^0_{n\sigma}(E)=$	$\frac{1}{2}+S_0$	$\frac{1}{2}-S_0$	$\frac{1}{2}-S_0$	$\frac{1}{2}+S_0$
$\int_{\rm v\ band}dE\rho^0_{n\sigma}(E)=$	$\frac{1}{2}-S_0$	$\frac{1}{2}+S_0$	$\frac{1}{2}+S_0$	$\frac{1}{2}-S_0$

A. Self-consistency of the antiferromagnetic background

The LDOS (local density of states) projected onto site n and spin direction σ, is defined in terms of the one-electron Green's function:

$$\rho^0_{n\sigma}(E)=\mathrm{sgn}(E)\frac{1}{\pi}\mathrm{Im}\ G^0_{\sigma\sigma}(n,n;E). \tag{2.2}$$

It is shown in Appendix A that

$$\rho^0_{n\sigma}(E)=\frac{\mathrm{sgn}(E)[E+(-1)^n\sigma US]}{\pi\sqrt{[E^2-(US)^2][(US)^2+4t^2-E^2]}} \tag{2.3}$$

for $US\leqslant|E|\leqslant\sqrt{(US)^2+4t^2}$ and 0 otherwise.

The total number of states per site per spin direction in each one of the bands can be calculated by integrating the LDOS over the corresponding ranges of energies. The results are shown in Table I.

Here,

$$S_0=\frac{US}{2N}\sum_k\frac{1}{E_k}. \tag{2.4}$$

In the ground state, at half-filling, there is one electron per site:

$$Q_n=\int_{\rm v\ band}dE(\rho^0_{n\uparrow}(E)+\rho^0_{n\downarrow}(E))=1.$$

Also, the spin at each site is given by

$$S^z_n=\frac{1}{2}\int_{\rm v\ band}dE(\rho^0_{n\uparrow}(E)-\rho^0_{n\downarrow}(E))=(-1)^{(n-1)}S_0,$$

$$S^x_n=0,\quad S^y_n=0.$$

This mean-field solution is made self-consistent, by requiring that the resulting spin S_o in Eq. (2.4) is equal to the assumed spin amplitude S.

Since E_k depends only on S^2, we can see that *the ground state is doubly degenerate*: both $+S$ and $-S$ satisfy Eq. (2.4) and give rise to self-consistent ground states that differ from each other only through the fact that all the spins are flipped from one ground state to the other one.

From Fig. 1(a), we can see that the dependence of S on U/t is as expected. In the weak interaction limit $U/t\ll1$, $S\to0$. The electrons have the same probability of spin up or down at any site (see table, for $S\to0$); the gap is closed and the electronic band is very broad ($4t$), showing that the electrons move freely (are delocalized) along the chain. In the strong interaction limit $U/t\gg1$, $S\to\frac{1}{2}$. The bands become very thin [$\sqrt{(US)^2+4t^2}-US\to2t\,(t/US)$], showing that

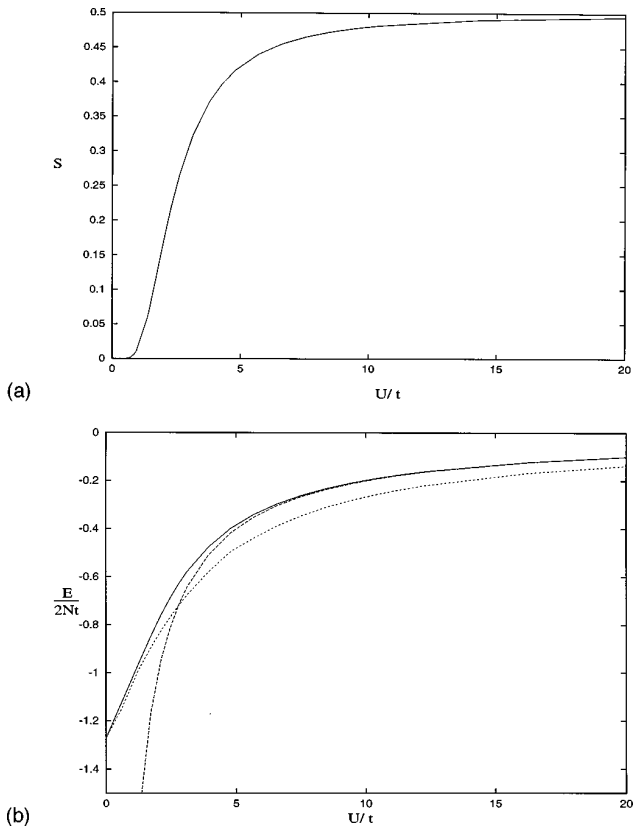

FIG. 1. (a) Magnitude S of the spin at a site as a function of U/t, in the AFM mean-field background. (b) Energy per site (in units of t) of the AFM mean-field background as a function of U/t (full line). The dotted line shows the prediction of the exact Lieb-Wu solution of the Hubbard model. The dashed line shows the asymptotic behavior $E/2Nt \rightarrow -2t/U$.

the electrons are strongly localized each at one site, each having its $\frac{1}{2}$ spin in the Oz direction. The AFM structure is energetically favorable since it allows a lowering of the energy by virtual hopping of electrons on their neighboring sites.

B. The energy of the antiferromagnetic background

Since all the states of the valence band are occupied, the energy of the AFM mean-field ground state is simply given by

$$E_{\rm gs}=2\sum_k E_k^v+2NU(S^2+\tfrac{1}{4}), \tag{2.5}$$

where $S=S_0$ in Eq. (2.4). The magnitude of the ground-state energy per site, in units of t, is plotted in Fig. 1(b) as a function of U/t (the full line). For comparison, the value predicted by the exact solution[29] of the 1D Hubbard model is also shown (dotted line). The following features can be observed: in the $U/t \rightarrow 0$ limit (noninteracting electrons), the energy of the ground state has, indeed, the expected value $E_{\rm gs}/2Nt \rightarrow -(4/\pi)$. In the strong interaction limit $U/t \rightarrow \infty$, the energy of the ground state goes to zero as expected (since in this limit every site is single occupied). The asymptotic value of our mean-field energy is found to be given by $E_{\rm gs}/2Nt \rightarrow -2(t/U)$ [see dashed line in Fig. 1(b)]. It is well known that in this limit, the Hubbard model is equivalent to an AFM Heisenberg model[30], with a coupling constant $J=4t^2/U$, and that its ground state energy per site[31] should be $E_{\rm gs}/2Nt \rightarrow -(J/t)\ln 2 = -2.77(t/U)$. This confirms that our mean-field method is a good starting point, from which to incorporate fluctuation corrections that lower the energy.

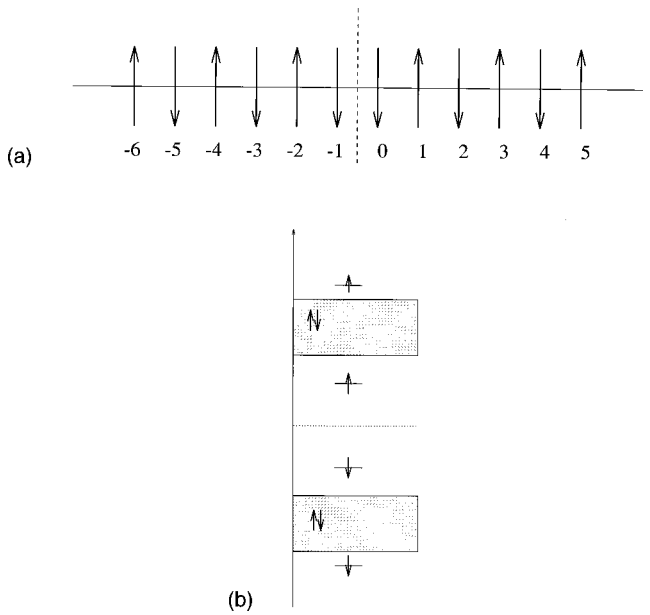

FIG. 2. (a) A sharp boundary soliton created by juxtaposition of regions found in the two AFM mean-field ground-states. (b) The electronic structure of the sharp boundary soliton consists of two spin-paired bands and four discrete nondegenerate levels within the gap. In the large U/t limit, the two strongly localized electrons occupying the gap levels corresponds to the two spins bordering the sharp boundary.

C. Neutral domain wall solitons

A sharp-boundary soliton is a domain wall consisting of a simple juxtaposition of two halves of the chain found in the two mean-field ground states (see Fig. 2). We treat this case in some detail, since it serves as ''reference case'' for more general extended solitons. Also, analytic calculations are possible and one can gain insight into the charge, spin, and statistics of such solitons.

The Green's functions for the Hamiltonian of the sharp-boundary soliton can be calculated analytically (see Appendix B). We summarize our results below.

In addition to the two Mott-Hubbard bands of the AFM mean-field background, there are also four nondegenerate discrete levels appearing in the gaps. Two of them occur inside the Mott-Hubbard gap ($|E|<US$),

$$E_{\uparrow}^{+}=-t+\sqrt{(US)^2+t^2}>0,$$

$$E_{\downarrow}^{-}=+t-\sqrt{(US)^2+t^2}<0$$

and the other two occur in the two external gaps [$|E|>\sqrt{4t^2+(US)^2}$]:

$$\tilde{E}_{\uparrow}^{+}=+t+\sqrt{(US)^2+t^2}>0,$$

$$\tilde{E}_{\downarrow}^{-}=-t-\sqrt{(US)^2+t^2}<0.$$

The spin projections for these nondegenerate levels are indicated in Fig. 2(b). This soliton preserves charge-conjugation symmetry: for each level of energy E and spin σ there is another level of energy $-E$ and spin $-\sigma$.

The spatial probability of localization on each of these four discrete levels is given by (see Appendix B):

$$|\phi_\sigma(n)|^2=\frac{1}{2\sqrt{1+\lambda^{-2}}}[\sqrt{\lambda^2+1}-\lambda]^{N(n)}, \qquad (2.6)$$

where $\lambda=US/t$, and

$$N(n)=N(-n-1)=\begin{cases} n & \text{if } n\geq 0 \text{ is even} \\ n+1 & \text{if } n\geq 0 \text{ is odd.}\end{cases}$$

Using the LDOS for the sharp-boundary chain, $\rho^s_{n\sigma}(E)$, derived in Appendix B, it follows, by straightforward integration, that

$$\int_{-\sqrt{(US)^2+4t^2}}^{-US} dE(\rho^s_{n\uparrow}(E)+\rho^s_{n\downarrow}(E))=1-2|\phi_\sigma(n)|^2.$$

Since there are exactly two discrete levels for $E<0$, this equation can be rewritten as

$$\int_{-\infty}^{0} dE(\rho^s_{n\uparrow}(E)+\rho^s_{n\downarrow}(E))=1. \qquad (2.7)$$

This shows that although the electronic structure is changed in the presence of the soliton, at half-filling all the electrons will occupy levels with $E<0$ (lowest energies available) and the sharp-boundary soliton is charge neutral: there is an average of one electron per site, exactly as in the ground state.

It is apparent from the above discussion that two localized states split off from each of the two bands and that there are an even number of states in the band after the creation of one sharp boundary soliton. The undoped soliton has all the levels with $E<0$ occupied. Since the valence band has an even number of states, half of which are spin up and half of which are spin down, the contribution of the band to the total spin is zero. There are also the two down spins that occupy the discrete levels. It follows that the total spin of the neutral soliton is an integer multiple of $\hbar$.

The sharp-boundary soliton provides a reference state from which we calculate self-consistent soliton structures. In the absence of anisotropy, the sharp-boundary soliton is unstable. Self-consistency for this reference state occurs only in the limit of $U/t\to\infty$.

In order to test the self-consistency of the soliton, we calculate the expectation value of the spin at every site, and compare it with the initial parameters. The evaluation of the corresponding integrals cannot be done analytically, except for the two sites near the boundary. It can be shown that the band contribution to these expectation values is exactly zero:

$$\frac{1}{2}\int_{-\sqrt{(US)^2+4t^2}}^{-US} dE(\rho^s_{n\uparrow}(E)-\rho^s_{n\downarrow}(E))=0, \text{ if } n=-1,0.$$

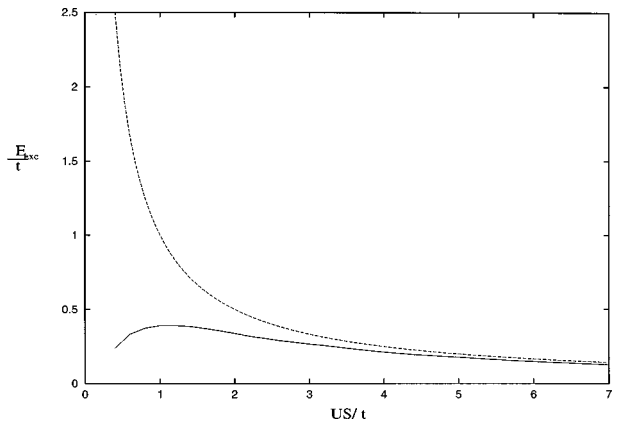

FIG. 3. Excitation energy (in units of t and measured with respect to the AFM mean-field background) of the sharp-boundary soliton, as a function of US/t. The dotted line shows the asymptotic value predicted by the Heisenberg model with $J=4t^2/U$.

This means that the entire contribution to the spin of these two sites comes from the two electrons in the occupied gap levels. The total spin at sites -1 and 0 is given by [see Eq. (2.6)]

$$S(-1)=S(0)=-\frac{US}{2\sqrt{(US)^2+t^2}}.$$

In the large US/t limit this approaches $-S=1/2$, and the picture becomes self-consistent. In this limit, the wave functions of the gap levels are very strongly localized near the boundary, and the two spins from the gap levels may be identified with the spins on either side of the boundary [see Figs. 2(a) and 2(b)]. This excitation is a boson, made up of two electrons occupying the gap levels.

The excitation energy necessary to create a sharp-boundary soliton is given by the difference between the soliton energy and the AFM background energy. This difference has two components, one coming from differences between expectation values of the electronic part $\mathcal{H}_{\rm el}$, and one coming from differences between the constants part $\mathcal{H}_{\rm const}$ [see Eqs. (1.4) and (1.5)]. For the sharp-boundary parameterization, the difference between the corresponding values of $\mathcal{H}_{\rm const}$ is zero, so that the excitation energy is given by

$$E^s_{\rm exc}=\sum_{n\sigma}\int_{-\infty}^{0} dE E\Delta\rho_{n\sigma}(E)$$
$$=\sum_{n\sigma}\int_{-\sqrt{(US)^2+4t^2}}^{-US} dE E\Delta\rho_{n\sigma}(E)+E^-_{\downarrow}+\tilde{E}^-_{\downarrow}. \qquad (2.8)$$

Here,

$$\Delta\rho_{n\sigma}(e)=\rho^s_{n\sigma}(E)-\rho^o_{n\sigma}(E)=\frac{1}{\pi}\mathrm{sgn}(E)\mathrm{Im}[G^s_{\sigma\sigma}(n,n;E)$$
$$-G^o_{\sigma\sigma}(n,n;E)]$$

represents the difference in the LDOS between the sharp-boundary soliton and the AFM background. This integral is evaluated numerically as a function of US/t in Fig. 3. As

expected, the energetic cost of exciting a sharp-boundary soliton decreases as $US/t \to \infty$; in this limit, the electrons are strongly localized and the interactions between them become very weak. From the equivalent Heisenberg model (valid in this limit), we know that the cost of exciting a sharp-boundary soliton must be $2JS^2 = J/2 = 2t^2/U$ (a pair of antiparallel spins becomes parallel, and $S = 1/2$ in this limit). The dashed line in Fig. 3 shows this asymptotic value, in agreement with our mean-field theory.

As in the case of Bloch walls that separate domains of ferromagnetism in conventional materials[32] such as iron, the AFM domain wall described above has an equilibrium thickness determined by the crystal *anisotropy* effects on the local magnetic moment orientation. For the isotropic tight-binding Hamiltonian (1.1), the neutral sharp-boundary soliton is unstable to relaxation into a gradual boundary in which the local moments in the core of the soliton rotate slowly from one AFM mean field at plus infinity to the other degenerate AFM mean field at minus infinity. Indeed, in the isotropic model, the minimum Hartree-Fock energy is realized when the soliton core radius approaches infinity. Nevertheless, we present a detailed study of the electronic structure of the neutral domain wall of the soliton. This provides a reference point for describing *stable, charged* domain wall solitons. The charged solitons have a finite equilibrium core radius that is determined by the subgap electronic structure that they induce, rather than anisotropy in the magnetic exchange interactions.

Consider the local magnetic moments of the extended neutral soliton on one sublattice (sublattice A). We allow these magnetic moments to slowly rotate from one AFM state, (with $\vec{S} = -S\vec{e}_z$, for instance), to the second AFM state, ($\vec{S} = S\vec{e}_z$) in the $(x0z)$ plane. The x direction is along the chain, and the rotation is characterized by an angle θ_n describing the expectation value of the spin at a site n: $\vec{S}_n = S(\cos\theta_n \vec{e}_x + \sin\theta_n \vec{e}_z)$. The angle θ_n varies from $-(\pi/2)$ to $(\pi/2)$ as n goes from $-\infty$ to $+\infty$, and is described by the ansatz $\theta_n = (\pi/2)\tanh[(n+0.5/\rho)]$, where ρ is the soliton core radius (in units of a). Here, the soliton is centered between the sites -1 and 0, as in the case of the sharp-boundary soliton.

Due to the symmetry of the problem, the rotation of the second sublattice (sublattice B) is described by the same angle θ_n. However, we are free to choose the sense of rotation. For the case that spins on the two sublattices rotate in the same sense [see Fig. 4(a)], we obtain

$$\vec{S}_n = S((-1)^{bn}\cos\theta_n \vec{e}_x + (-1)^n \sin\theta_n \vec{e}_z) \tag{2.9}$$

with $b = 1$. In this case the spins remain locally antiparallel everywhere along the chain, we call this excitation an *AFM-core soliton*.

The second possibility is when the spins on the two sublattices rotate in opposite senses [see Fig. 4(b)]. In this case we use formula (2.9) except with the choice $b = 0$. In this case spins in the core of the soliton become parallel and we call such an excitation a *FM-core soliton*.

The corresponding mean field Hamiltonian is given by

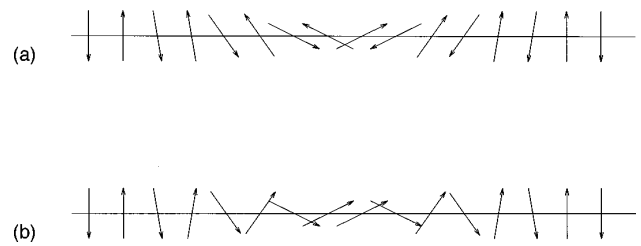

FIG. 4. (a) Structure of an AFM-core soliton. The spins on the two sublattices rotate from one mean-field ground state to the other one, preserving the local antiferromagnetic correlations. (b) Structure of the FM-core soliton. The spins on the two sublattices rotate in opposite directions, creating a ferromagnetic region in the core of this soliton.

$$\mathcal{H}^b_{\rm el} = -t\sum_{\langle i,j\rangle}(\chi_i^\dagger \chi_j + \text{H.c}) - US\sum_i \chi_i^\dagger((-1)^{bi}\cos\theta_i \sigma_x + (-1)^i \sin\theta_i \sigma_z)\chi_i, \tag{2.10}$$

where $\chi_i^\dagger = (\hat{a}_{i\uparrow}^\dagger \hat{a}_{i\downarrow}^\dagger)$.

$H_{\rm const}$ has the same expression as in Eq. (1.5) and has exactly the same value as in the mean-field ground state case, since the magnitude of the spin at each site remains S and there is one electron per site.

The Green's function associated with Eq. (2.10) is evaluated using Dyson's equation, with the sharp-boundary soliton as a reference case.

We write

$$\mathcal{H}^b_{\rm el} = \mathcal{H}^s_{\rm el} + V^b,$$

where $\mathcal{H}^s_{\rm el}$ is the electronic part of the Hamiltonian of the sharp-boundary soliton. V^b is a potential localized near the core of the soliton, on a region characterized by the core radius of the soliton. This potential is diagonal in the site space, but not in the spin space. The Dyson equations for the Green's functions are given by

$$G^b_{\sigma\sigma'}(n,m;E) = \delta_{\sigma\sigma'} G^s_{\sigma\sigma}(n,m;E) + \sum_{p\sigma''} G^s_{\sigma\sigma}(n,p;E) V^b_{\sigma\sigma''}(p) G^b_{\sigma''\sigma'}(p,m;E). \tag{2.11}$$

Here, we have used the fact that G^s is diagonal in spin space. Once the values of $G^b_{\sigma\sigma'}(n,n;E)$ are known at any site n, we can calculate physical quantities such as the LDOS, the excitation energy of the soliton and the expectation value of the spin at various sites (see Appendix B).

D. Electronic states in the gap

In the presence of a sharp-boundary soliton, four electronic levels split from the valence and conduction band, and become localized levels in the gap. For extended solitons, the number of such gap levels and their energies vary as a function of the soliton core radius. In Figs. 5(a) and 5(b) we plot the electronic spectrum (bands and discrete levels) as a function of the soliton core radius for the two types of solitons, for a fixed value of the Mott-Hubbard gap US/t.

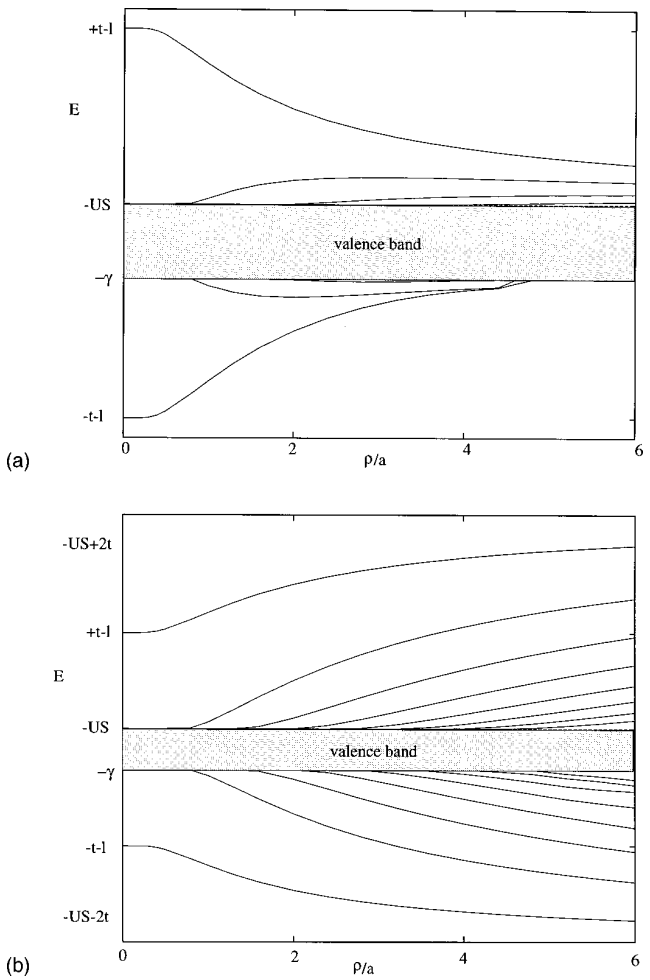

FIG. 5. (a) The lower half of the electronic spectrum of an AFM-core soliton, as a function of the soliton core radius ρ. In the limit $\rho\to 0$, there are two discrete levels. In the limit $\rho\to\infty$, this soliton becomes indistinguishable from the mean-field background. As the soliton core radius ρ increases, the discrete levels reenter the bands. (b) The lower half of the electronic spectrum of a FM-core soliton, as a function of the soliton core radius ρ. In the limit $\rho\to 0$, there are two discrete levels. In the limit $\rho\to\infty$, the entire chain becomes ferromagnetic and the spectrum consists of two continuum bands, the valence band corresponding to $E\in[-US-2t,-US+2t]$. Here $\gamma=[4t^2+(US)^2]^{1/2}$ and $l=[t^2+(US)^2]^{1/2}$.

In the $\rho\to 0$ limit, both solitons show the same structure, as the sharp-boundary soliton. However, as ρ increases, the behavior of the two spectra is very different. For the FM-core soliton, more and more levels split off from both bands and go deeper into the gaps. For the AFM-core soliton the tendency is opposite: the gap levels go toward and eventually reenter the bands. These different behaviors can be understood if we analyze the $\rho\to\infty$ limit. In this limit, an AFM-core soliton is practically indistinguishable from the ground state, because the rotation angle between spins on neighboring unit cells goes to zero. Therefore, the electronic structure should become identical with that of the ground state, which consists only of the two bands. This is exactly the behavior seen in Fig. 5(a). On the other hand, in the presence of a FM-core soliton with $\rho\to\infty$, all the chain is in the core region, which is a perfect FM state. The electronic structure of

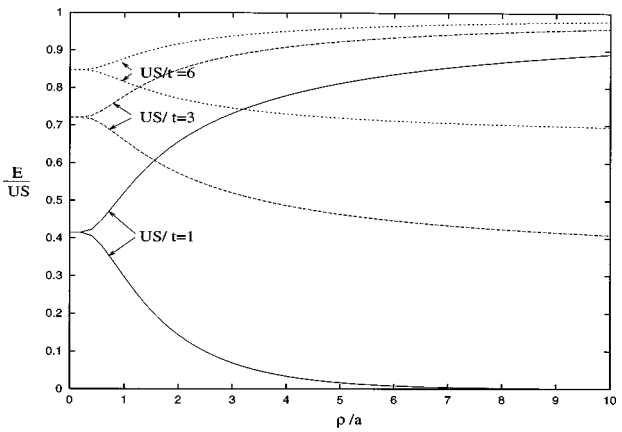

FIG. 6. The energy of the near midgap ($E>0$) level for the undoped FM- and AFM-core soliton, for $US/t=1$, 3, and 6, as a function of the soliton core radius. For the FM-core soliton this level approaches the midgap, while for the AFM-core soliton it approaches the band edge. For $US/t<2$, the FM-core soliton level reaches the midgap. For $US/t>2$, this level goes to $US-2t$, the band edge of the FM valence band.

a FM state can be easily calculated, and it is seen that it is made up of two bands with energies $E\in[-US-2t,-US+2t]$ and $E\in[US-2t,US+2t]$, the lower (valence) band consisting of nondegenerate levels with spins in the direction of the FM spins ($+Ox$ direction, in this case), while the upper (conduction) band consists of nondegenerate levels with spins in the opposite direction. This shows that as ρ increases, the initial AFM bands containing doubly degenerate levels with up and down spins in the Oz direction will spread out into the broader FM bands with spins in the Ox direction. This spreading of the bands as ρ increases is shown in Fig. 5(b).

The most interesting gap levels are the pair of levels closest to the midgap, because these levels accommodate the doping electrons or holes. In Fig. 6 we show the behavior of one of these levels ($E>0$) for different values of US/t, as a function of ρ. There are two distinct types of behavior and two different regimes for the FM soliton. If $US/t<2$, the level reaches the midgap, while if $US/t>2$ the level goes to some nonzero value as $\rho\to\infty$. This is consistent with the band structure of the FM state. This state has an inner gap for energies $E\in[-US+2t,US-2t]$, which is consistent with the fact that if $US/2t>1$, the gap level goes to $\pm(US-2t)\neq 0$. If $US/2t<1$, the gap is closed in the FM core. Therefore the gap level goes to $E=0$ as ρ increases.

E. Excitation energies of the neutral solitons

We now evaluate the total density of states (DOS) and the excitation energy of the solitons. If $\mathcal{H}^s_{\rm el}$ and $\rho^s(E)$ are the Hamiltonian and total density of states, respectively, of the sharp-boundary soliton, then the difference between the total densities of states of the chain with an extended soliton and the chain with a sharp-boundary soliton is given by[33]

$$\Delta\rho(E)=\rho^b(E)-\rho^s(E)=\frac{1}{\pi}\,\mathrm{Im}\frac{d}{dE}\ln\det[1-V^bG^s(E)]. \tag{2.12}$$

Since V^b has nonzero matrix elements only for a finite range of sites, the determinant can be calculated in the site-spin basis, and is equal to the determinant of the finite region with non-vanishing matrix elements of V^b. Introducing the function

$$F(E) = \mathrm{Im}\{\ln[\det(1 - V^b G^s(E))]\}, \tag{2.13}$$

the variation of the DOS is given by

$$\Delta\rho(E) = \frac{1}{\pi}\frac{d}{dE}F(E). \tag{2.14}$$

The difference between the energies of the ground states of $\mathcal{H}^s_{\mathrm{el}}$ and $\mathcal{H}^b_{\mathrm{el}}$ can be expressed in terms of $F(E)$:

$$\Delta E_{\mathrm{gs}} = \int_{\mathrm{occ\ states}} E\Delta\rho(E)dE = -\frac{1}{\pi}\int_{\mathrm{occ\ states}} F(E)dE. \tag{2.15}$$

In writing the last equality, we made use of the fact that the chemical potentials of both Hamiltonians are equal ($\mu=0$ in both undoped cases). In the undoped case there is no contribution to the excitation energy coming from $\mathcal{H}_{\mathrm{const}}$ part, since it has the same value for the extended solitons as for the ground state. For the doped case, the gap levels that are occupied (or empty) have to be taken into account as well.

The total excitation energy relative to the uniform AFM background is given by

$$E_{\mathrm{exc}} = -\frac{1}{\pi}\int_{\mathrm{occ\ states}} F(E)dE + E^s_{\mathrm{exc}} \tag{2.16}$$

where E^s_{exc} is given in Eq. (2.8). For a fixed value of US/t, the typical variation of E_{exc} with ρ is shown in Fig. 7(a). In the $\rho\to 0$ limit, both the FM-core and AFM-core solitons behave identically and their excitation energies equal that of the sharp-boundary soliton. As ρ increases, the excitation energy of the AFM-core soliton decreases, since as $\rho\to\infty$ this soliton merges into the AFM background. On the other hand, the excitation energy of the FM-core solitons increases with ρ, since as the core size increases, more spins become parallel instead of antiparallel.

The instability of the neutral domain wall soliton is a general characteristic of 1D systems. As in the classical theory of Bloch walls separating domains of magnetization in a ferromagnet, a stable finite-core-size soliton can exist if crystal anisotropy energies are included in the model. Nevertheless, the importance of these domain walls is apparent. For a doped system it is energetically more advantageous to pay the cost of creating a domain wall and lower the total energy by allowing the doping electron (hole) to occupy a deep gap level than it would be to let the doping electron (hole) occupy the first available level in the conduction band. In the next section, we identify two types of charged solitons on the lattice with different spin and statistics from conventional charge carriers in a metal. The lowest-energy charged soliton, which is centered *on* a site, appears to be a spinless bosonic excitation. A charged soliton which is centered *between* two sites has higher energy and appears to be an *unstable* spin-1/2 fermion for $US/t>2$, whereas for $US/t<2$ it has the character of a spinless boson.

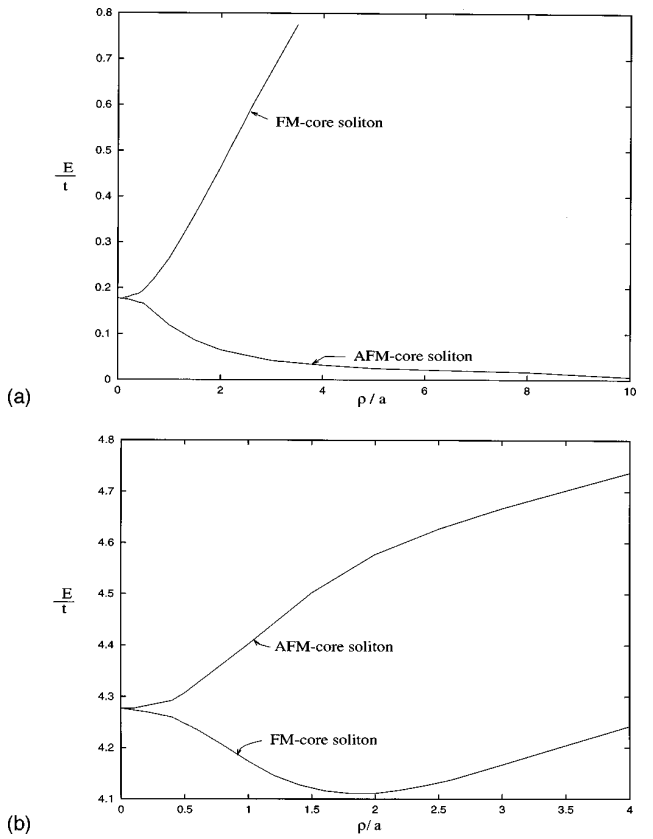

FIG. 7. (a) Excitation energies (in units of t and measured with respect to the AFM mean-field background) of the undoped FM-core soliton and AFM-core soliton, as a function of the soliton core radius ρ. Here $US/t=5$. In the absence of magnetic anisotropy the 1D neutral domain wall is unstable; the minimum energy occurs for $\rho\to\infty$. (b) Excitation energies (in units of t and measured with respect to the AFM mean-field background) of a doped FM/AFM-core soliton, as a function of the soliton core radius ρ. This estimate is obtained by adding the energy of the level occupied by the doping electron (hole) to the excitation energy of the undoped soliton. For $US/t=5$, a stable, charged FM-core soliton exists at $\rho/a=2$.

III. CHARGED DOMAIN WALL SOLITONS

By adding the energy of the first available gap level of an undoped FM/AFM-core soliton to the total excitation energy of the undoped FM/AFM-core soliton, we obtain a first estimate of the excitation energy of a doped FM/AFM-core soliton. The typical dependence with the core radius of this energy (in units of t), for a given US/t, is shown in Fig. 7(b). This offers plausibility to the idea that a charged FM-core soliton is stable at a finite-core radius. It suggests that the doped soliton excitation energy is indeed less than US [which is the energetic cost of placing the electron (hole) on the first available level in the conduction (valence) band, in the absence of the soliton]. However, this elementary consideration is not self-consistent. Adding an electron (hole) on the first available level in the gap (i.e., in a localized state) modifies the expectation values of the spin in the core of the soliton. In order to get a self-consistent model, we proceed as follows. We start with the initial parameters of an undoped soliton and calculate the corresponding Green's functions (in the way described in the previous section). The expectation values of the spin of the corresponding doped soliton at vari-

ous sites are obtained by integrating, over the correct range of energies, the trace of the imaginary part of the Green's function at that site multiplied by the $\vec{\sigma}$ operator (in spin space). This yields a new set of spin expectation values. Once these new parameters are obtained, the next iteration begins, and the process continues until it converges to a self-consistent solution.

A. Self-consistent charged solitons

Remarkably, the self-consistent, Hartree-Fock, structure of the charged soliton does not exhibit spiral twist of the magnetic background as suggested by the structure of the extended neutral solitons. Instead, the charged soliton consists of a collinear spin alignment in which the magnitude of the local magnetic moment is suppressed within the soliton core. Using the procedure described above, we calculate the self-consistent shape, electronic spectra, and excitation energies of the charged solitons. For both self-consistent solutions, the magnitude of the spin along the chain becomes zero $S_n^x=0$, while the spin perpendicular to the chain is suppressed in the core of the soliton. The vanishing of the component parallel to the chain has a simple interpretation. In the neutral soliton, the main contribution to the spin parallel to the chain was given by the electron on the deepest occupied gap level, and it is exactly this level that becomes empty upon hole doping.

The two self-consistent charged solitons are depicted in Fig. 8. The magnitude of the spin perpendicular to the chain is well approximated by $S_n^z=S\tanh(n+0.5/\rho)$ for a doped soliton centered between two sites, and $S_n^z=S\tanh(n/\rho)$ for a doped soliton centered at a site. In Fig. 9(a) we plot the self-consistent soliton core radius for both solitons as a function of US/t. In the large US/t limit, the localization length of the gap levels is very small and accordingly the soliton itself is very small. In the small US/t limit, the bound levels are more extended, and the solitons are large. For large solitons, a continuum approximation that we discuss in the next section recaptures the lattice results, and there is no distinction between the two types of solitons. This can be seen from Figs. 9(b) and 9(c). In Fig. 9(b) we plot the excitation energies of the two types of solitons (in units of t, and defined with respect to the undoped AFM mean-field background) as a function of US/t. In the small US/t limit, the two excitation energies are practically equal [and very well approximated by the value of $US/\sqrt{2}t$ predicted by the continuum model (dotted line)]. In the intermediate and large US/t regimes the size of the soliton becomes comparable to the lattice constant. In this case the doped soliton centered at a site is energetically favorable to the doped soliton centered between sites. For any value of US/t, the excitation energy of both types of solitons is less than US, the energetic cost of simply adding the doping electron (hole) on the first available level in the conduction (valence) band. This suggests that charged solitons must appear automatically on the chain upon doping.

In Fig. 9(c) we plot the lower half of the electronic spectra of the two types of solitons (these doped solitons have discrete levels only in the internal gap, and they have the usual charge-conjugation symmetry). *The doped soliton centered at a site has only a doubly degenerate level at the midgap for any value of* US/t. Using symmetry arguments, it is easy to see that this level is empty (or doubly occupied) for the hole (electron) doped soliton. The spectrum of the doped soliton centered between two sites is more complicated: for $US/t<2$, there are only two nondegenerate levels symmetric with respect to $E=0$, which go to zero as $US/t\to 0$. Since the soliton is doped, these levels are either both occupied or both empty. For $US/t>2$, a new pair of nondegenerate levels splits off the inner band edges and becomes localized. The spin projections of these nondegenerate gap levels are similar to those of the sharp-boundary soliton: the two lower levels support down spins (more generally, spins pointing in the same direction as the expectation values of the spin at the two sites near the center of the soliton), while the two upper levels have the opposite projection. The appearance of this second pair of gap levels has important consequences, related to the spin of such a soliton. We discuss this issue below.

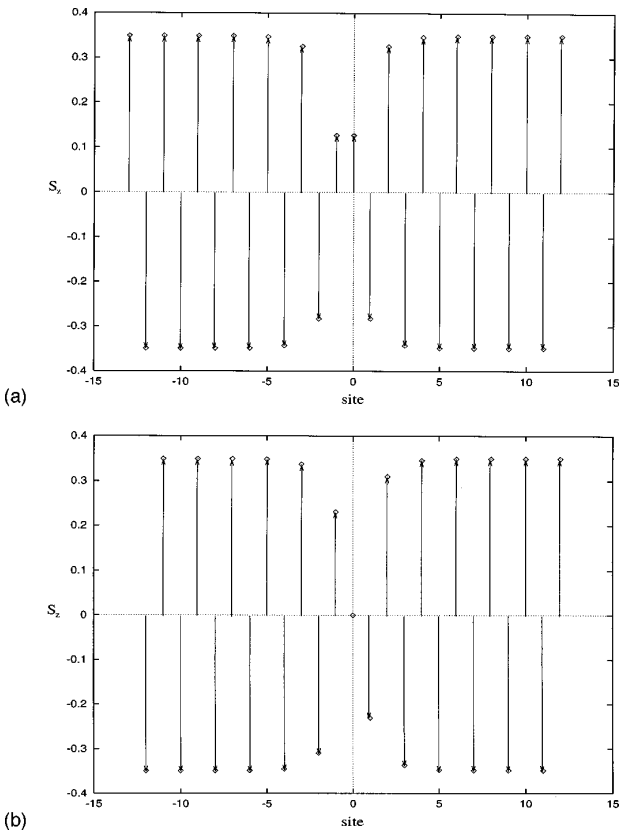

FIG. 8. (a) The self-consistent spin distribution of a doped soliton centered between sites. Here, $US/t=1.2$. The magnitude of the spin is suppressed in the core of the soliton, due to the localization of the doping particle in the core. (b) Same as (a) for doped soliton centered at a site.

B. Spin of the charged soliton

The doped soliton centered at a site is a boson. This can be seen from its electronic spectrum: all the states in the continuum bands are spin paired and filled, while the doubly degenerate midgap level is either empty or doubly occupied. This means that the total projection of the spin perpendicular to the chain is zero. Therefore this soliton is a charged boson.

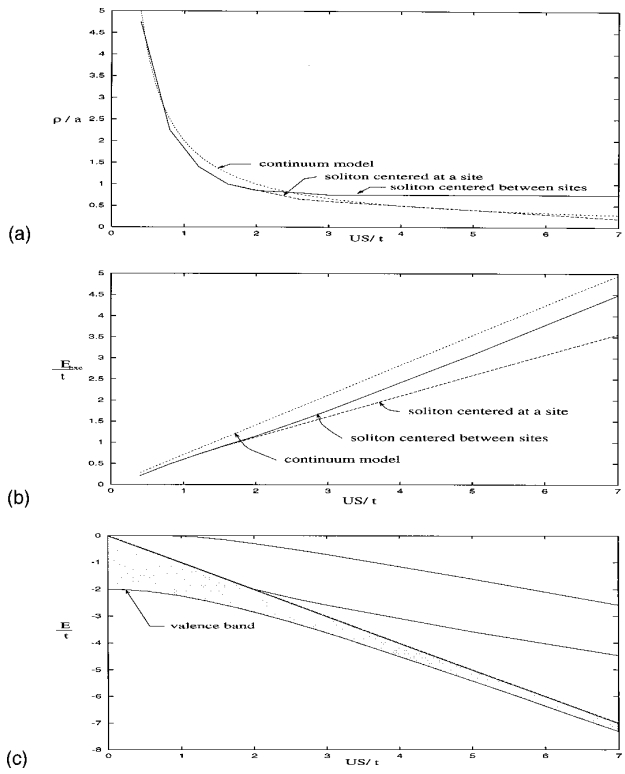

FIG. 9. (a) Soliton core radius of a self-consistent doped soliton centered at a site (full line) and centered between sites (dashed line), as a function of US/t. (b) The excitation energies (in units of t) of the self-consistent doped soliton centered between sites (full line) and centered at a site (dashed line), as a function of US/t. For $US/t<2$, the soliton core radii are large and the two solitons become indistinguishable, giving excellent agreement with the continuum model (dotted line). For $US/t>2$, the soliton radius is comparable to the lattice constant. (c) Electronic spectra of the self-consistent doped solitons as a function of US/t. The soliton centered at a site has a doubly degenerate midgap level for all US/t. For $US/t<2$, the soliton centered between sites has a pair of nondegenerate levels which go towards the midgap as US/t decreases. For $US/t>2$, a second pair of nondegenerate levels split from the bands.

In the small US/t limit this is confirmed by the continuum model (see next section). The fact that the total spin of the doped soliton is zero can be seen also from Fig. 8(b). By symmetry, the sum of the spins to the left of the core must be equal and opposite to the sum of the spins to the right of the soliton, giving a vanishing total spin.

The situation of the doped soliton centered between sites is more complicated. For $US/t<2$, this soliton is a boson, because it has the same type of electronic structure as the other soliton. On the other hand, for $US/t>2$, this soliton is a fermion. Since a new nondegenerate level splits from the lower band edge, this lower discrete level is occupied by one electron. While this level was still in the valence band ($US/t<2$) its spin was delocalized over the whole chain. Therefore it did not contribute to the spin of the soliton. As this level goes deeper and deeper into the gap, the corresponding wave function becomes well localized in the core of the soliton, and the 1/2 spin it carries becomes the spin of the soliton. Another way to understand the fermionic character of this soliton for large US/t is to start from the undoped sharp-boundary model analyzed previously, and dope it. We have argued that in the strongly localized limit, the two electrons occupying the two discrete levels with $E<0$ of the sharp-boundary soliton contribute equally to the spins of the two sites bordering the center of the soliton. The total spin of the undoped soliton is an integer multiple of $\hbar$. As we remove one of these electrons, in order to get a doped soliton centered between sites, the magnitude of the spin at the two sites bordering the center decreases by half, leaving behind a total spin of 1/2.

The bosonic charged soliton centered on a site is energetically favored and it can lower its energy further by quantum-mechanical hopping along the chain. Since the structure of this soliton is unchanged (in the large US/t limit) as the hole moves, this type of soliton is very mobile and its total energy is lowered by an amount of the order of t as it moves. The doped soliton centered between two sites is a charged fermion. This soliton, however, is relatively immobile, since motion requires changes in the magnitudes of the spins even for large US/t.

C. Charge density of the doped solitons

In the previous sections, we simplified the eigenvalue spectrum of the charged solitons by neglecting the charge density term in the mean-field Hamiltonian (1.4). A self-consistent treatment of the charge density leads to a loss of (charge conjugation) symmetry of the soliton eigenvalue spectrum about $E=0$. However, the general conclusions concerning the charge and the spin of the solitons remains the same as discussed earlier. In order to take into consideration this extra charge localized in the core of the soliton, we use the Hamiltonian (1.4) to describe the doped system. The self-consistent calculations once again yield two types of doped solitons.

Although the charged soliton centered at a site continues to have a doubly degenerate gap level, the charged solitons centered between sites has only nondegenerate gap levels. However, their spectra are no longer symmetric with respect to $E=0$. Instead, this symmetry manifests in a more subtle way. Let $\mathcal{H}_{\rm el}^{\rm hole}$ be the Hamiltonian of a hole-doped soliton defined by the parameters $\vec{S}_n$ and $Q_n=1-\Delta\rho_n$, and $\mathcal{H}_{\rm el}^{\rm electron}$ the Hamiltonian of an electron-doped soliton defined by the parameters $-\vec{S}_n$ and $Q_n=1+\Delta\rho_n$. (This is exactly the type of correspondence expected in systems with charge-conjugation symmetry.) It is straightforward to prove that if $\phi_{\rm hole}(n)$ is a spinor such that $\mathcal{H}_{\rm el}^{\rm hole}\phi_{\rm hole}(n)=E\phi_{\rm hole}(n)$, then the spinor $\phi_{\rm electron}(n)=(-1)^n\phi_{\rm hole}(n)$ satisfies the equation $\mathcal{H}_{\rm el}^{\rm electron}\phi_{\rm electron}(n)=-E\phi_{\rm electron}(n)$. In other words, the electronic spectrum of the hole-doped soliton is obtained by reflection with respect to $E=0$ from the electronic spectrum of the electron-doped soliton.

This loss of symmetry of the electronic spectrum makes the problem of determining the Fermi level nontrivial. It turns out that the chemical potential remains fixed at zero, as was the case for the undoped soliton. In other words, for a hole (electron) doped soliton all the $2N-1$ $(2N+1)$ occupied states (where N is number of unit cells of the chain) are below $E<0$. This symmetry guarantees that the ''shapes'' of the self-consistent electron- and hole-doped solitons are the same. The spin distribution is not greatly modified by the charge term. The tanh function still gives a good fit, and the

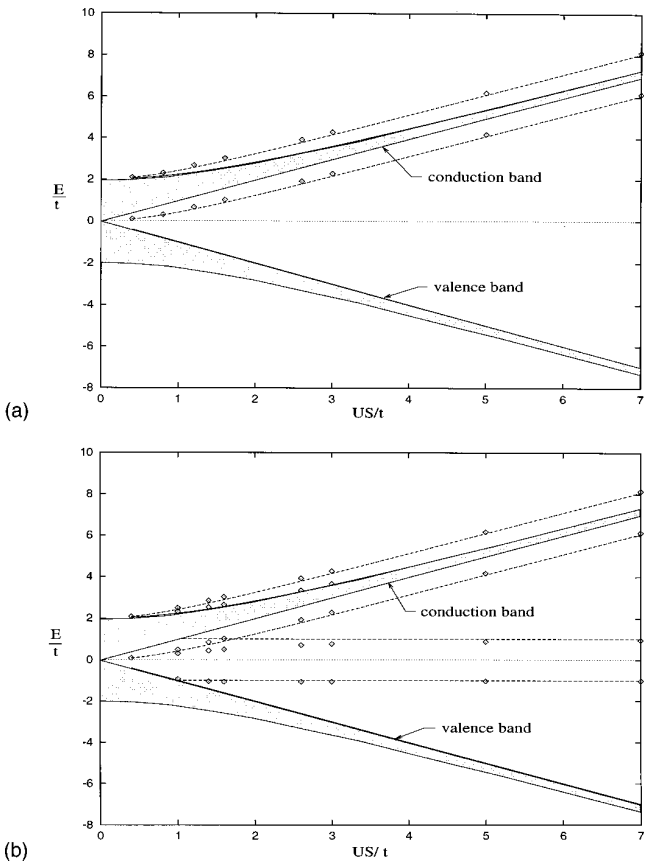

FIG. 10. (a) Electronic spectrum of a hole-doped soliton centered at a site including charge redistribution effects, as a function of US/t (diamonds). All gap levels are doubly degenerate. The lines show the approximate values found in the large US limit. All levels below the midgap are occupied. (b) Same as (a) for a hole-doped soliton centered between sites. All gap levels are nondegenerate. The spectra of the corresponding electron-doped solitons are obtained by inversion with respect to $E=0$.

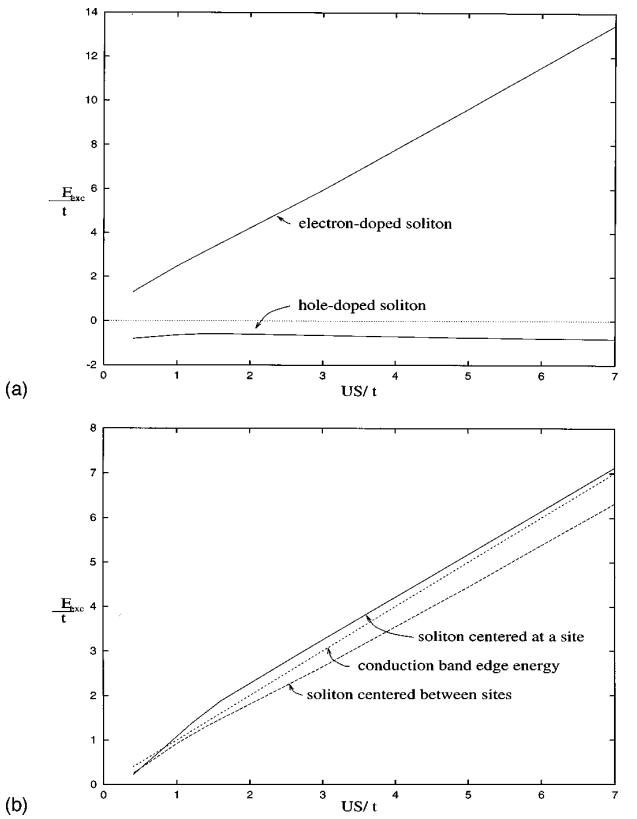

FIG. 11. (a) Excitation energies (in units of t) of static hole- and electron-doped solitons centered at a site, as a function of US/t, with no compensating positive background. (b) Excitation energies (in units of t) of static doped solitons centered at a site (full line) and centered between sites (dashed line), as a function of US/t, with a uniform, compensating positive background. The solitons centered at a site can move freely along the chain, and therefore their actual energy is lowered by an amount $2t$ relative to the static soliton.

soliton core radii have the same qualitative behavior as in the previous case. The electronic spectra of the hole-doped solitons centered between sites and centered at one site are shown in Figs. 10(a) and 10(b) (the spectra of the corresponding electron-doped solitons are obtained by reflection with respect to $E=0$). All the gap levels of the doped soliton centered between sites are nondegenerate, while the gap levels of the doped soliton centered at a site are doubly degenerate.

From Fig. 10(a), we can see that the doped soliton centered at a site remains a charged boson, since only levels below $E=0$ are occupied. For a hole-doped soliton centered at a site, only the valence-band levels are occupied and there is no possibility of a localized spin. For the electron-doped soliton centered at a site, all the degenerate gap levels are doubly occupied, and once again there is complete spin cancellation.

For the doped soliton centered between sites, we see again two distinct behaviors. For a hole-doped soliton centered at a site, we see from Fig. 10(b) that below $US/t=1$ there are no gap levels with $E<0$. Therefore only the levels of the valence band are occupied and this doped soliton must be a boson. For $US/t>1$, a discrete level splits off the band edge of the valence band and becomes a bound state, carrying a 1/2 spin that makes this soliton a fermion. Similarly, the electron-doped soliton centered between sites is seen to be a fermion for $US/t>3$, where there are three occupied gap levels, and a boson below $US/t<3$, where there are four occupied gap levels.

In the large US/t limit, we find a simple analytic expression to describe the approximate position of the discrete levels of these solitons. For the hole-doped soliton centered at a site, the positions of the two doubly degenerate gap levels are well approximated by $E=\sqrt{(US)^2+t^2}\pm t$, while for the hole-doped soliton centered between sites, the two levels near the midgap are at $\pm t$ while the two upper levels are at $\sqrt{(US)^2+t^2}\pm t$ [see dotted lines in Figs. 10(a) and 10(b)].

The total energies of the self-consistent electron- and hole-doped solitons are shown in Fig. 11(a). The resulting excitation energy of the hole-doped solitons (lower line), which is lower than the excitation energy of the electron-doped solitons (the upper line), is an artifact of our Hamiltonian that does not contain a term describing Coulomb attraction between the electrons and the positive background nuclei. This artificially favors a hole-doped soliton. An electron-doped soliton costs more energy, in this oversimplified model, because the extra repulsive energy due to having more electrons is not compensated by attraction between the

extra electron and the nuclei. The contribution of a neutralizing positive background may be estimated by simply taking the average between the excitation energies of the hole-doped soliton and the electron-doped soliton. This is shown in Fig. 11(b) for the two types of doped solitons. The important observation about Fig. 11(b) is that the average energy of the electron- and hole-doped soliton centered at a site, exceeds US. However, it should be remembered that this soliton can lower its energy by an amount t by quantum-mechanical hopping motion along the chain [this is one unit on the vertical scale of Fig. 11(b)]. This additional mobility for the charged soliton centered on a site makes it energetically favorable compared to the soliton centered between sites.

The increase in the excitation energy of the doped solitons when the charge terms are included is partly an artifact of the purely on-site Coulomb repulsion of the Hubbard model. For an electron-doped soliton centered at a site, the extra electron is basically localized on top of another electron, and this costs an enormous amount of energy. A more realistic model should consider a longer-range Coulomb interactions as well as a more realistic model for the positive background charge of the nuclei.

IV. CONTINUUM MODELS

The properties of lattice solitons, which we have described so far, can be elegantly recaptured by means of a continuum model. The appropriate continuum model is constructed in such a way that the local antiferromagnetic correlation between nearest-neighbor sites is treated exactly, but fluctuations from one unit cell (consisting of two spins) to another have slow spatial variations. This also provides a foundation for constructing the appropriate continuum model for the two-dimensional antiferromagnet (described in Sec. V) where the lattice model is very cumbersome.

One of the difficulties of a discrete model is that the eigenequations $H\phi(n)=E\phi(n)$ are recurrence relations. In the continuum model, these recurrence relations are replaced by differential equations, which in turn have analytical solutions. The simplest continuum approximation consists of expanding the dispersion relations near the Brillouin-zone edge $k_0=\pm\pi/2a$. If we expand the free-electron dispersion relations $\epsilon_k=2t\cos(ka)$ near this point, we get the approximate value $\epsilon_k=-2ta(k-k_0)$. Changing the reference point from $k=0$ to $k=k_0$ in the reciprocal space, we can write

$$\epsilon_k \underset{k\to k_0}{\to} -2tak=2tai\frac{d}{dx}.$$

The hopping Hamiltonian can then be approximated by (see Appendix A)

$$\mathcal{H}_{\rm ke}=-\sum_k \Phi_k^\dagger\begin{pmatrix}0 & -2tak\\ -2tak & 0\end{pmatrix}\Phi_k$$

$$=\int dx\ \Phi^\dagger(x)\left(-2tai\tau_x\frac{d}{dx}\right)\Phi(x). \qquad (4.1a)$$

In what follows, the Pauli matrices $\sigma_{x,y,z}$ are associated to the spin space, while the Pauli matrices $\tau_{x,y,z}$ are associated to the site space. Here $\Phi(x)$ is a four-component spinor describing the two components of electron spin on each of the two lattice sites constituting a unit cell. Similarly, the interaction part of the Hamiltonian becomes

$$\mathcal{H}_{\rm int}=\int dx\Phi^\dagger(x)\left[-U\cdot\begin{pmatrix}\vec{S}_1(x)\cdot\vec{\sigma} & 0\\ 0 & \vec{S}_2(x)\cdot\vec{\sigma}\end{pmatrix}\right.$$

$$\left.+\frac{U}{2}[1-Q(x)]\right]\Phi(x), \qquad (4.1b)$$

where $\vec{S}_{1(2)}$ is the expectation value of the spin at the site 1(2) of the unit cell located at x, and $Q(x)$ is the charge at a site.

In the undoped case, we can use the same parametrization as for the discrete case. $Q(x)=1$ for both the AFM-core and the FM-core solitons. However,

$$\vec{S}_1(x)=S(\cos[\theta(x)]\vec{e}_x+\sin[\theta(x)]\vec{e}_z),$$

$$\vec{S}_2(x)=S((-1)^b\cos[\theta(x)]\vec{e}_x-\sin[\theta(x)]\vec{e}_z).$$

For an AFM-core soliton, we choose $b=1$, whereas for the FM-core soliton we choose $b=0$. Here $\theta(x)$ describes the direction of the local spin with respect to the chain axis. The continuum Hamiltonian for the AFM/FM-core soliton is given by

$$\mathcal{H}=\int dx\Phi(x)^\dagger\left\{-2tai\tau_x\frac{d}{dx}\right.$$

$$\left.-USA\tau_z(\sin\theta A\sigma_z+\cos\theta\sigma_x)\right\}\Phi(x), \qquad (4.2)$$

where $A=1$ for the AFM-core soliton and $A=\tau_z$ for the FM-core soliton.

The electronic structure of the mean-field, AFM background states $[\theta(x)=\pm\pi/2]$ of this Hamiltonian is made up of two bands whose dispersion relations are $E_k^{(\pm)}=\pm\sqrt{(US)^2+4a^2t^2k^2}$, and a Mott-Hubbard gap of magnitude $2US$. In the presence of a soliton, the angle $\theta(x)$ describes the rotation between the two ground states, and is characterized by a soliton core radius ρ. We choose

$$\theta(x)=\frac{\pi}{2}\tanh\left(\frac{x}{\rho}\right). \qquad (4.3)$$

Introducing the dimensionless variables,

$$\zeta=x\frac{US}{2at},\quad e=\frac{E}{US},\quad \text{and}\ \ \rho_c=\rho\frac{US}{2at},$$

the soliton spectrum is obtained by solving the eigenvalue problem,

$$\left\{-i\tau_x\frac{d}{d\zeta}-\tau_z(\sin\theta(\zeta)\sigma_z+A\cos\theta(\zeta)\sigma_x)\right\}\phi(\zeta)=e\phi(\zeta), \qquad (4.4)$$

where $\theta(\zeta)=(\pi/2)\tanh(\zeta/\rho_c)$. Unlike the lattice model, in which there are two independent parameters US/t and ρ/a, here we have just one parameter ρ_c.

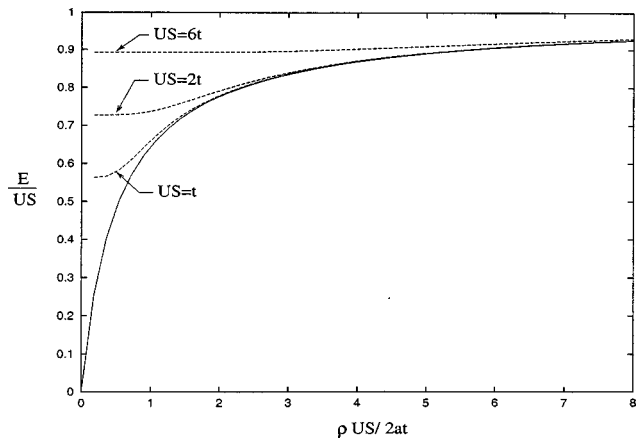

FIG. 12. Dependence of the energy of the discrete gap level on $\rho_c = \rho US/2at$, predicted by the continuum model (full line), and by the discrete models with $US/t = 1,\ 2$, and 6, for an AFM-core soliton.

A. AFM-core soliton

Since the AFM-core soliton Hamiltonian commutes with the operator $P = \tau_x \sigma_y$, the eigenfunctions $\phi(\zeta)$ can be chosen to be eigenfunctions of P as well. Since $P^2 = 1$ and P is hermitian, its eigenvalues are ± 1. We perform a unitary transformation with $U = \exp[-i(\pi/4)\,\tau_y \sigma_y]$ such that P becomes diagonal, i.e., $U^{-1} P U = \tau_z$. Labeling the eigenvalues of τ_z by $s = \pm 1$, we obtain the differential equation for the new two-component function $\eta(\zeta) = U\phi(\zeta)$:

$$\left[-i\sigma_y \frac{d}{d\zeta} - [\cos\ \theta(\zeta)\sigma_x + \sin\ \theta(\zeta)\sigma_z] \right] \eta(\zeta) = se\,\eta(\zeta). \tag{4.5}$$

This shows that if there is a level with the quantum numbers (e,s) there is another level with the quantum numbers $(-e,-s)$, as expected for charge-conjugation invariance. Clearly, the discrete levels on either side of the midgap have different parities. We can see from the structure of Eq. (4.5) that the levels are nondegenerate, since there is no matrix that anticommutes with all three Pauli matrices.

Using the method presented in Ref. 13, we numerically evaluate the gap structure. There are only two levels in the gap, with energies varying from 0 to the band edges, as ρ_c varies from zero to infinity. In Fig. 12 we present a comparison between the results of the continuum model with that of the discrete AFM-core soliton model for various values of US/t. In the large ρ_c limit the agreement is very good for many choices of US/t. For small ρ_c values, the agreement is best when US/t is small as expected, since for a given ρ_c, smaller US/t values correspond to bigger ρ/a values.

The excitation energy of the continuum AFM soliton is similar to that of the lattice AFM soliton. The band contribution to the total soliton energy varies slowly with ρ_c, leaving the main contribution to the discrete levels. For the undoped soliton, only the discrete level with $E<0$ is occupied, and the energy of this level decreases as ρ_c increases. As the soliton expands, its excitation energy diminishes, until it becomes indistinguishable from the AFM mean-field background.

B. FM-core soliton

Since the FM-core soliton Hamiltonian commutes with the operator $P = \tau_x \sigma_x$ (with eigenvalues ± 1), the eigenfunctions $\phi(\zeta)$ can be chosen such that they are eigenfunctions of P as well. We perform a unitary transformation with $U = \exp[-i(\pi/4)\,\tau_y \sigma_x]$ such that $U^{-1} P U = \tau_z$. Once again, labeling the eigenvalues of τ_z by $s = \pm 1$, we obtain the differential equation for the new two-component function $\eta(\zeta) = U\phi(\zeta)$:

$$\left[-is\sigma_x \frac{d}{d\zeta} - [\cos\ \theta(\zeta)\sigma_x + s\ \sin\ \theta(\zeta)\sigma_z] \right] \eta(\zeta) = e\,\eta(\zeta). \tag{4.6}$$

For the FM-core soliton (unlike the AFM-core soliton), the matrix σ_y anticommutes with the Hamiltonian. Therefore, if there is a state ϕ with the quantum numbers (e,s), then there is another state $\sigma_y \phi$ with the quantum numbers $(-e,s)$ as expected by charge-conjugation invariance. Another difference is that for the FM-core soliton, levels with energies in the different halves of the gap have the same parity (instead of opposite parity for AFM soliton). Using the same argument as before, there are no degenerate discrete levels, except at $e = 0$. This is verified by numerical calculations. Numerically, we find only a doubly degenerate level at $e = 0$, and the corresponding wave function is given by

$$\eta_s(\zeta) = C \begin{pmatrix} 1 \\ -i \end{pmatrix} \exp\left(-\int_0^{\zeta} d\zeta' (\sin\ \theta(\zeta') + is\ \cos\ \theta(\zeta')) \right), \qquad s = \pm 1. \tag{4.7}$$

Here, C is a normalization constant.

C. Self-consistent theory of the doped soliton in the continuum model

In the case of doped solitons, a self-consistent solution for the spin degrees of freedom is possible if we take $Q(x) = 1$. The self-consistent solution of the discrete case suggests a parametrization of the form $\vec{S}_1(x) = -\vec{S}_2(x) = S\ \tanh(x/\rho)\vec{e}_z$. It turns out that with this parametrization, the continuum model has a simple analytical solution. In fact, it maps onto the continuum polyacetylene model.[27] The total ''electronic'' Hamiltonian is given by

$$\mathcal{H}_{\rm el} = \int dx \Phi^{\dagger}(x) \left\{ -2tai\tau_x \frac{d}{dx} - US\tau_z \sigma_z \tanh\frac{x}{\rho} \right\} \Phi(x). \tag{4.8}$$

Using the dimensionless variables defined earlier, the eigenvalue problem reduces to

$$\left\{ -i\tau_x \frac{d}{d\zeta} - \tanh\left(\frac{\zeta}{\rho_c}\right) \tau_z \sigma_z \right\} \phi(\zeta) = e\,\phi(\zeta). \tag{4.9}$$

Using the fact that the Hamiltonian commutes with σ_z, and introducing the quantum number s [defined by $\sigma_z \phi_s(\zeta) = s\,\phi_s(\zeta)$], Eq. (4.9) reduces to a pair of two-component equations:

$$\left\{ -i\tau_x \frac{d}{d\zeta} - s \tanh\left(\frac{\zeta}{\rho_c}\right)\tau_z \right\} \phi_s(\zeta) = e\phi_s(\zeta), s = \pm 1. \tag{4.10}$$

This equation can be written in a more familiar form if we perform a rotation by $\pi/2$ about the Oy axis in the site space. This rotation is implemented by the matrix $U = \exp[-i(\pi/4)\tau_y]$. The rotated Hamiltonian $\mathcal{H} = U^\dagger \mathcal{H}_{\rm el} U$ and the rotated wave function $\psi_s(\zeta) = U^\dagger \phi_s(\zeta)$ satisfy the equation

$$\left\{ -i\tau_z \frac{d}{d\zeta} + s \tanh\left(\frac{\zeta}{\rho_c}\right)\tau_x \right\} \psi_s(\zeta) = e\psi_s(\zeta). \tag{4.11}$$

For $s=1$, this equation is identical to the corresponding equation for charged solitons in polyacetylene [Eq. (7) from Ref. 27]. From Eq. (4.11) we can see that $\psi_{-1}(\zeta) = \tau_z \psi_{+1}(\zeta)$. Therefore, for $s=-1$ we obtain the same spectrum.

The above considerations demonstrate that the spectrum of this doped soliton is identical to the spectrum of the soliton in polyacetylene. In the polyacetylene case, the spin is a trivial degree of freedom and consequently each level is doubly degenerate. The soliton structure induces phase shifts in the band wave functions and, therefore, the calculation of the excitation energy of the doped FM-core soliton follows exactly the same steps described in Ref. 27. This yields the result that the doped soliton is stable when $\rho_c = 1$ or $\rho/a = 2t/US$. In this particular case, the spectrum of the soliton is made up of a doubly degenerate level at the midgap plus the two bands. The soliton excitation energy is given by $US/\sqrt{2}$. The results of the continuum model are in good agreement with the results of the lattice model in the small US limit [see Figs. 9(a) and 9(b)].

It is straightforward to verify that this calculation is self-consistent with respect to the expectation value of the spin. The band wave functions are given by

$$\psi_{+1,k}(\zeta) = \begin{pmatrix} u_k(\zeta) \\ v_k(\zeta) \end{pmatrix} \quad \text{and} \quad \psi_{-1,k}(\zeta) = \begin{pmatrix} u_k(\zeta) \\ -v_k(\zeta) \end{pmatrix},$$

where the detailed expressions for $u_k(\zeta)$ and $v_k(\zeta)$ in the case $\rho_c = 1$ are given in Ref. 27. Explicitly, we have even solutions,

$$u_k(\zeta) + iv_k(\zeta) = \sqrt{\frac{2}{L}} \frac{1}{1+ik} [k \cos k\zeta - \tanh\zeta \sin k\zeta],$$
$$u_k(\zeta) - iv_k(\zeta) = \sqrt{\frac{2}{L}} i \sqrt{\frac{1-ik}{1+ik}} \sin k\zeta,$$

and odd solutions,

$$u_k(\zeta) + iv_k(\zeta) = \sqrt{\frac{2}{L}} \frac{1}{1+ik} [k \sin k\zeta + \tanh\zeta \cos k\zeta],$$
$$u_k(\zeta) - iv_k(\zeta) = \sqrt{\frac{2}{L}} (-i) \sqrt{\frac{1-ik}{1+ik}} \cos k\zeta.$$

Here, the dimensionless wave vector $k \geq 0$ is measured in units of $US/2at$.

Rotating these wave functions back to the initial representation, we obtain the band wave function:

$$\phi^*_{+1,k}(\zeta) = \frac{1}{\sqrt{2}} [u^*_k(\zeta) - v^*_k(\zeta), 0, u^*_k(\zeta) + v^*_k(\zeta), 0], \tag{4.12}$$

$$\phi^*_{-1,k}(\zeta) = \frac{1}{\sqrt{2}} [0, u^*_k(\zeta) + v^*_k(\zeta), 0, u^*_k(\zeta) - v^*_k(\zeta)].$$

The wave functions of the two midgap levels are given by

$$\phi^*_{+1,B}(x) = \frac{1}{2\sqrt{\rho}\cosh(x/\rho)} (-1, 0, -i, 0), \tag{4.13}$$

$$\phi^*_{-1,B}(x) = \frac{1}{2\sqrt{\rho}\cosh(x/\rho)} (0, i, 0, 1).$$

In the doped soliton, all the levels in the valence band are occupied, and the midgap levels are either empty or doubly occupied. Therefore, the only contribution to the expectation value of the spins comes from the band. Using these wave functions, the expectation value of the spin in the z direction is given by

$$S_z(\zeta) = \tfrac{1}{4} \langle \tau_z \sigma_z \rangle_{\rm band} = \tfrac{1}{4} \sum_{s,k} \phi^*_{s,k}(\zeta) \tau_z \sigma_z \phi_{s,k}(\zeta)$$
$$= -\sum_k \mathrm{Re}[u^*_k(\zeta) v_k(\zeta)] = S \tanh(\zeta), \tag{4.14}$$

where $S = (1/2L) \Sigma_k [US/\sqrt{(US)^2 + 4a^2t^2k^2}]$ and $L = 2Na$ is the length of the chain. This demonstrates the self-consistency, since we have shown previously that the magnitude S satisfies this condition (recall the self-consistency equation for the AFM mean-field background). The expectation values for the spin in the x and y directions are zero.

It is straightforward to verify that this doped soliton has no spin, but carries the charge of the doping electron (hole). For each energy level in the band, there are an equal number of eigenfunctions with up ($s=+1$) and down ($s=-1$) spin σ_z. Since all the levels in the band are occupied, the total spin is zero. On the other hand, the doped soliton has a charge $\pm e$, which is localized in the core region with a probability density given by that of the midgap level. For a hole-doped soliton only the valence band is occupied and the expectation value of the probability (charge) density is given by

$$\rho(x) = \sum_{k,s} \phi^*_{s,k} \phi_{s,k} = 2 \sum_k (|u_k|^2 + |v_k|^2)$$
$$= \frac{1}{a} \left[1 - \frac{1}{2\cosh^2(x/\rho)} \cdot \frac{\tan^{-1}\pi(t/US)}{\pi(t/US)} \right]. \tag{4.15}$$

The total charge (in units of the electron charge) at one site is given by $Q(x) = a\rho(x)$. The total number of electrons in the chain is given by

$$\int_{-L/2}^{L/2} \rho(x)dx = 2N - \frac{2}{\pi} \tan^{-1}\left(\pi \frac{t}{US}\right),$$

where $L=2Na$ is the length of the chain and N is the number of unit cells. In the limit $US/t\to 0$ (weak coupling), this goes indeed to $2N-1$, as expected for one extra hole.

V. TWO-DIMENSIONAL ANTIFERROMAGNET: ELECTRONIC STRUCTURE OF MERON VORTICES

In this section we demonstrate the analogy between 1D domain walls and polarons, and 2D merons and skyrmions, respectively, in the continuum approximation. In order to keep the article self-contained, we review the main points in the derivation of the 2D continuum Hamiltonian.

As discussed in Sec. I, we assume that the 2D lattice Hamiltonian is given by Eq. (1.4). The mean-field background consists of antiferromagnetically aligned local magnetic moments whose Hartree-Fock energy has been lowered by the inclusion of uniform spin flux. This is expressed formally by setting the product of the electron hopping matrices $T^{12}T^{23}T^{34}T^{41}=-1$ around any elementary plaquette. We choose the simplest spin-independent gauge in which $T^{ij}=-1$ for one link of each plaquette, but $T^{ij}=1$ for the remaining three links. The spectrum is independent of the choice of the gauge. For undoped solitons we choose $Q_i=1$ and, since we are interested only in the electronic spectra, we drop the constant terms.

We introduce an eight-component annihilation operator $\phi(\vec{r})$ for up- and down-spin electrons at the four sites of the square unit cell located at $\vec{r}$, and the corresponding eight-component Bloch operator $\phi_{\vec{k}}=N^{-1/2}\Sigma_{\vec{r}}e^{-i\vec{k}\vec{r}}\phi(\vec{r})$. Here N is the number of unit cells and the sum is performed over all the unit cells. $\vec{k}$ is restricted to the first Brillouin zone, which in this case is defined by $k_x\in[-\pi/2a,\pi/2a]$, $k_y\in[-\pi/2a,\pi/2a]$. In terms of the Bloch operators, the Hamiltonian can be rewritten as

$$\mathcal{H}=\sum_{\vec{k}}\phi_{\vec{k}}^{+}[\epsilon_{k_x}\alpha_x+\epsilon_{k_y}\alpha_y+U\beta]\phi_{\vec{k}}, \tag{5.1}$$

where $\epsilon_k=-2t\cos ka$, a is the lattice constant, and α_x,α_y and β are 8×8 matrices whose structure is dependent on our choice for the mean-field parameters T^{ij} and $\vec{S}_i$. Explicitly,[14]

$$\alpha_x=\begin{pmatrix}0&(T^{12})^{+}&0&0\\T^{12}&0&0&0\\0&0&0&(T^{34})^{+}\\0&0&T^{34}&0\end{pmatrix}=-\gamma_z\otimes\tau_x\otimes I, \tag{5.2a}$$

$$\alpha_y=\begin{pmatrix}0&0&0&T^{41}\\0&0&(T^{23})^{+}&0\\0&T^{23}&0&0\\(T^{41})^{+}&0&0&0\end{pmatrix}=\gamma_x\otimes\tau_x\otimes I,$$

where we choose $T^{12}=-1$, $T^{23}=T^{34}=T^{41}=1$. Here I is the 2×2 identity matrix in the spin space, and $\vec{\gamma}$ and $\vec{\tau}$ are two sets of 2×2 Pauli matrices describing hopping in the x and y directions, respectively. We will use the $\vec{\sigma}$ Pauli matrices to describe the internal spin-space of the electron. These matrices appear in the interaction term,

$$\beta=\begin{pmatrix}\vec{S}_1\vec{\sigma}&0&0&0\\0&\vec{S}_2\vec{\sigma}&0&0\\0&0&\vec{S}_3\vec{\sigma}&0\\0&0&0&\vec{S}_4\vec{\sigma}\end{pmatrix}, \tag{5.2b}$$

where $\vec{S}_i$ describes the expectation value of the spin at the i site of the unit cell.

In the AFM mean-field reference state we have $\beta=S\tau_z\sigma_z$ (assuming that the spins are oriented in the z direction), and the dispersion relations are given by

$$E_{\vec{k}}=\pm\sqrt{(\epsilon_{k_x}^2+\epsilon_{k_y}^2)+(US)^2}. \tag{5.3}$$

Due to the relativistic form of the dispersion relations, the Fermi surface at half-filling ($E_F=0$) collapses to the four corner points of the Brillouin zone, $\vec{k}^o=[\pm(\pi/2a),\pm(\pi/2a)]$. The continuum approximation consists, as in the 1D case, in linearizing the electron-dispersion relations about one of these isolated Fermi points, by replacing $\cos(k_ia)$ with $(k_i-k_i^o)a\to -ia\partial_i$, $i=x,y$.

Using the dimensionless variables $x\to x\,(US/2at)$, $y\to y\,(US/2at)$, and $E\to(E/US)$, the Schrödinger equation becomes

$$\left[i\alpha_x\partial_x+i\alpha_y\partial_y+\frac{1}{S}\beta\right]\psi(\vec{r})=E\psi(\vec{r}). \tag{5.4}$$

As in the case of the domain walls in one dimension, there are two distinct types of meron-vortex configurations in two dimensions. For a meron with an AFM core we may parametrize the interaction matrix β by the relations

$$\vec{S}_1=-\vec{S}_2=\vec{S}_3=-\vec{S}_4=S\hat{n}. \tag{5.5}$$

Here,

$$\hat{n}=[\sin\theta(r)\cos(\mu\phi),\sin\theta(r)\sin(\mu\phi),\cos\theta(r))$$

plays the role of a plaquette director field, around which there are four antiferromagnetically correlated local moments. For the FM-core meron, the required parameterization is given by

$$\vec{S}_1=\vec{S}_3=S\hat{n},\qquad \vec{S}_2=\vec{S}_4=-S(\hat{n}-2\hat{n}_z). \tag{5.6}$$

Here, μ is the vortex winding number and we choose the angle $\theta(r)=2\tan^{-1}(r/\rho)$ for $r<\rho$ and $\theta(r)=(\pi/2)$ for $r>\rho$. The angle of the plaquette director field with respect to the z axis varies from 0, in the core of the meron, to $\pi/2$, in the asymptotic region, as shown in Fig. 13.

It is straightforward to see that the two merons have the same asymptotic structure, but their cores are very different: while for the AFM-core soliton the spins are antiferromagnetically aligned on each unit cell and rotate slowly in the same direction as the plaquette vector, for the FM-core soliton spins on the two sublattices rotate in opposite directions,

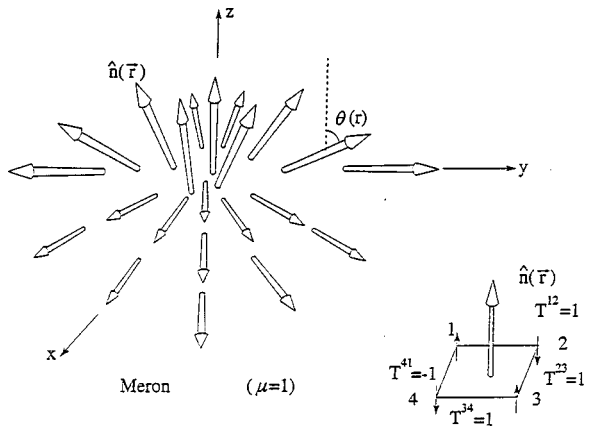

FIG. 13. The 2D analog of the neutral domain wall is a meron texture depicted as a lotus-flower configuration of the local director field $\hat{n}(\vec{r})$. As $\hat{n}(\vec{r})$ varies smoothly from one unit cell to the next, it makes a half-covering of the unit sphere S_2. If the meron is doped, all the components of the spin perpendicular to the plane become zero, and therefore the magnitude of the spin vanishes in the core of the charged meron vortex.

such that they become parallel (ferromagnetic) in the core of the soliton. With these parametrizations we have

$$\beta = S\tau_z \sin\,\theta(r)[\cos(\mu\phi)\sigma_x + \sin(\mu\phi)\sigma_y] + SA\,\tau_z \cos\,\theta(r)\sigma_z = SA\,\tau_z U^{+}(\vec{r})\sigma_z U(\vec{r}), \quad (5.7)$$

where $U(\vec{r}) = e^{i\theta(r)A\sigma_y/2} e^{i\mu\phi\sigma_z/2}$. Here, $A=1$ for an AFM-core meron, while $A=\tau_z$ for a FM-core meron.

In polar coordinates, the kinetic energy terms reduce to

$$i\alpha_x\partial_x + i\alpha_y\partial_y = e^{-i(\phi/2)\alpha_z}\left[i\alpha_x\left(\partial_r + \frac{1}{2r}\right) + i\alpha_y\frac{\partial_\phi}{r}\right] e^{i(\phi/2)\alpha_z},$$

where $\alpha_z = -\gamma_z$. With this choice, the three α matrices satisfy the cyclic algebra $[\alpha_i,\alpha_j] = i\epsilon_{ijk}\alpha_k$. We introduce a radial wave function $\eta(r)$, defined by $\phi(\vec{r}) = e^{i(\alpha_x+\mu\sigma_z+2l)\phi/2}\eta(r)/\sqrt{r}$, to obtain the radial Schrödinger equation,

$$\left[i\alpha_x\partial_r + \frac{\alpha_y}{r}\left(\frac{\mu}{2}\sigma_z + \ell\right) + A\,\tau_z\sigma(r)\right]\eta(r) = e\,\eta(r). \quad (5.8)$$

Here, $\sigma(r) \equiv e^{-i\theta A\sigma_y/2}\sigma_z e^{i\theta A\sigma_y/2}$ and ℓ is an angular momentum quantum number. Since we are using the dimensionless variables $r \to r\,(US/2ta)$ and $E \to e = E/US$, the only independent parameter is $\rho\,(US/2ta)$, as in the 1D case. Since the meron does not carry additional spin flux, only integer values of ℓ are allowed. The solution of this equation can be simplified by noting that the plaquette parity operator $P \equiv \tau_z\gamma_y$ commutes with H_r. It follows that the eigenfunctions of H_r can be labeled according to the eigenvalues of P, which we denote as $s_1 = \pm 1$. Introducing the unitary matrix $U_1 = e^{i(\pi/4)\gamma_x\tau_z}$, and noting the $U_1^{+} P U_1 = \gamma_z$, the transformed radial equation becomes

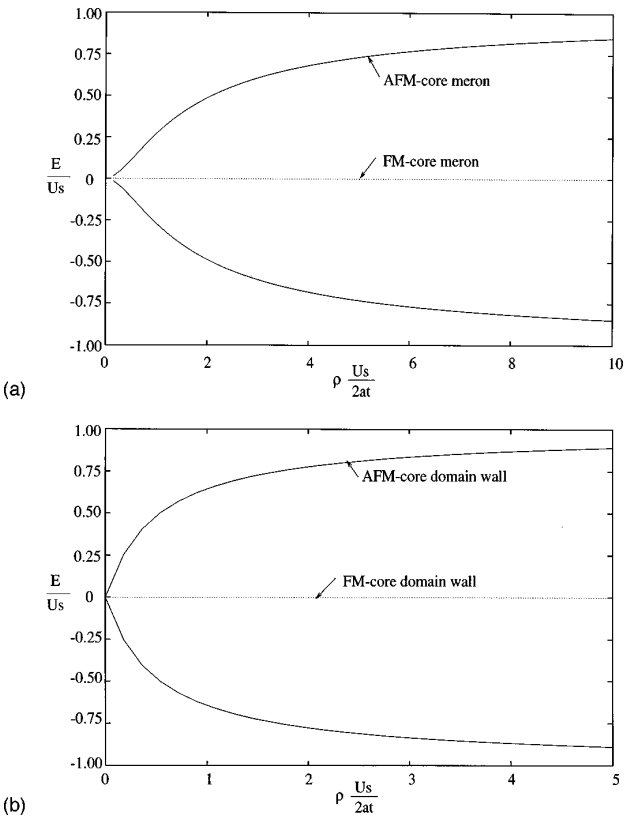

FIG. 14. (a) Electronic gap structure of the FM- and AFM-core 2D merons as a function of the continuum parameter $\rho US/2at$, as predicted by the continuum model. (b) Electronic gap structure of the FM- and AFM-core 1D domain walls as a function of the continuum parameter $\rho US/2at$, as predicted by the continuum model.

$$\left\{ -is_1\tau_x\partial_r + \frac{\tau_y}{r}\left(\frac{\mu}{2}\sigma_z + \ell\right) + A\,\tau_z(\sigma_z\cos\,\theta + \sigma_x A\,\sin\,\theta)\right\}\eta = E\,\eta. \quad (5.9)$$

For either the FM-core or AFM-core solitons, if η is an eigenfunction of Eq. (6) with quantum numbers (E,s_1,ℓ), it follows that $\sigma_y\eta$ is another eigenfunction with quantum numbers $(-E,-s_1,-\ell)$. Therefore the spectrum is always symmetric about $E=0$. For the AFM-core soliton $(A=I)$, it follows that $\tau_x\eta$ is another eigenfunction with quantum numbers $(-E,-s_1,\ell)$. As a consequence, the $\ell \neq 0$ levels of the AFM-core solitons are doubly degenerate whereas the $\ell = 0$ levels are nondegenerate. For the FM-core soliton $(A=\tau_z)$, the state $\tau_y\sigma_z\eta$ is another eigenfunction with quantum numbers $(E,-s_1,\ell)$. As a consequence, all of the levels of the FM-core soliton are doubly degenerate. We can see that for $\ell = 0$ the structure of the levels and the quantum numbers associated with them are analogous to the 1D case. In the AFM structure, for every state labeled by quantum numbers (E,s_1) there is another state $(-E,-s_1)$. In the FM structure, for every state (E,s_1) there is another state $(-E,s_1)$.

Numerical calculations also give a very similar gap structure, as shown in Fig. 14. The AFM-core meron has two nondegenerate gap levels with opposite parity, which go towards the midgap as $\rho\,(US/2at) \to 0$ and towards the band edges in the limit $\rho\,(US/2at) \to \infty$. *The FM-core meron has*

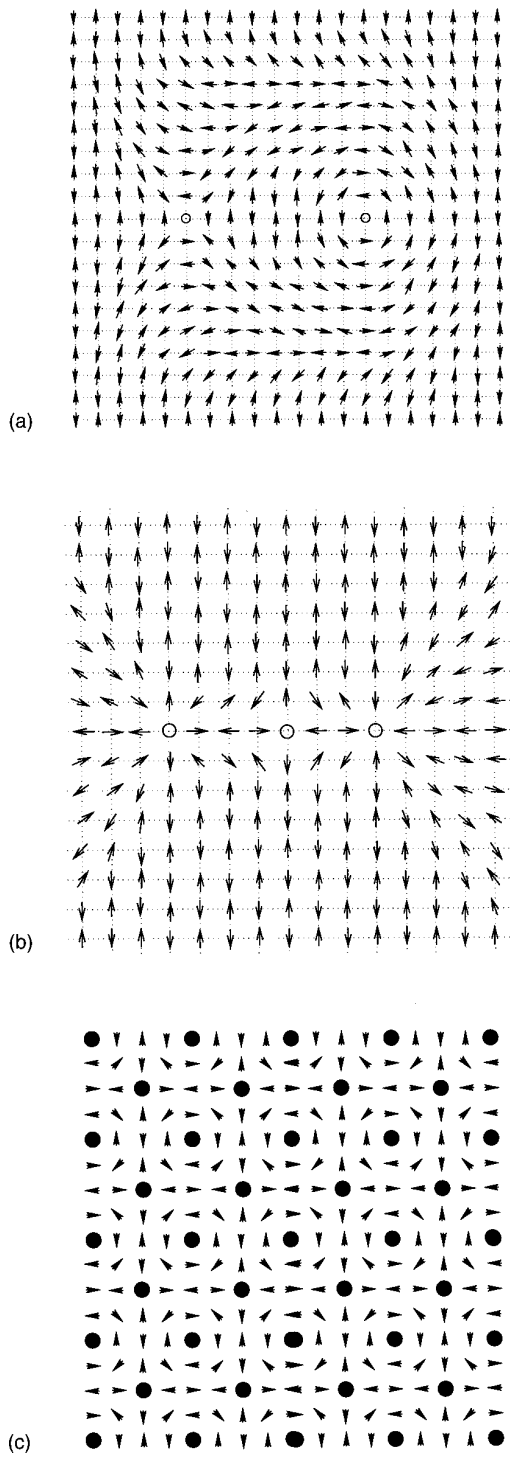

FIG. 15. (a) A pair of charged merons with the winding number $\mu=1$ and $\mu=-1$. The AFM mean-field background is distorted only over a finite region. (b) Creation of the backbone of a horizontal charged stripe. (c) Meron crystal corresponding to the hole concentration $\delta=1/8$. This configuration may be responsible for the suppression of superconductivity in some compounds, at this concentration.

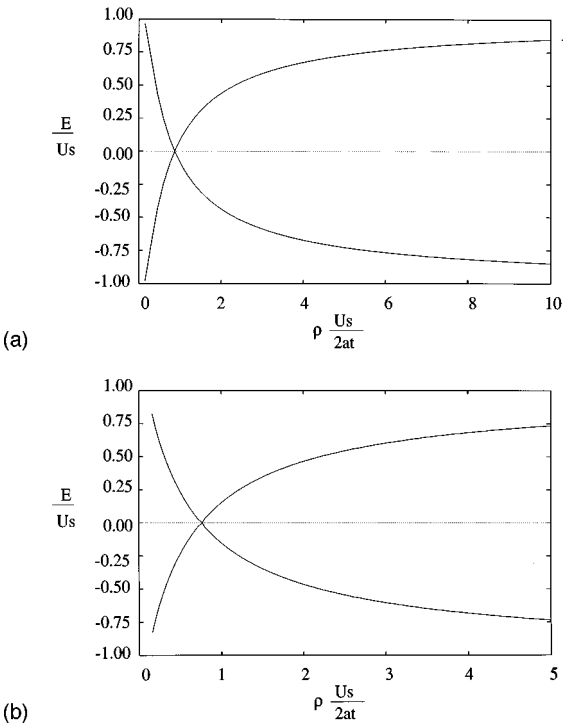

FIG. 16. (a) Electronic gap structure of the FM- and AFM-core 2D skyrmion as a function of the continuum parameter $\rho US/2at$, as predicted by the continuum model. (b) Electronic gap structure of the FM- and AFM-core 1D polaron as a function of the continuum parameter $\rho US/2at$, as predicted by the continuum model.

a doubly degenerate level at the midgap. This close similarity between the 1D and 2D structures can be seen for other magnetic textures as well. In particular, the 2D skyrmion structure is analogous to the 1D polaron. The 1D polaron may be regarded as a bound pair of domain wall solitons and the 2D skyrmion is topologically equivalent to a bound pair of merons [see Fig. 15(a)]. For the skyrmion we choose $\theta(r)=2\tan^{-1}(r/\rho)$ and for the polaron we choose $\theta(x)=2\tan^{-1}(x/\rho)$. In this case, a truly FM core does not exist, since at $r=0(x=0)$ the arrangements of the spins of a unit cell is the same as that of a unit cell in the asymptotic region, except that all spins are flipped. In the asymptotic region we have an AFM arrangement. This means that in the core we have an AFM arrangement as well. Consequently we can set $A=1$ in Eq. (5.9). All the symmetries of the Hamiltonian remain as for the meron (domain wall), and in the large $\rho(US/2at)$ limit the band structure is basically the same. It consists of two nondegenerate levels that go towards the band edges. In the small $\rho(US/2at)$ limit, the levels cross over and go towards the opposite band edge, instead of going towards the midgap [see Figs. 16(a) and 16(b)].

Finally, we discuss the nature of the charged meron, obtained by doping the 2D antiferromagnet with a hole. In analogy with the charged domain wall soliton in 1D we expect that the local magnetic moment amplitude in the core of the meron will be suppressed. The undoped meron has a ''lotus-flower'' structure (see Fig. 13). It resembles a planar vortex in the plaquette director field in the asymptotic region. In the core region, the plaquette vector points in a direction perpendicular to the 2D plane. In analogy with the doped 1D soliton, we assume that the effect of doping the 2D meron is simply to remove the components of spin perpendicular to the plane, and the ''lotus flower'' is reduced to a planar vortex in which the local moment amplitude vanishes in the core region. Remarkably, for this charged meron-vortex configuration, it is possible to obtain an analytic solution for the

midgap electronic structure. We set $\cos\theta \equiv 0$ and we take the same ''doped'' parameterization $\sin\theta = \tanh(r/\rho)$. It is straightforward to show that the meron radial equation has a doubly degenerate midgap level, whose wave functions are given, up to a normalization constant, by

$$\eta^*(r) = \sqrt{r}\ \mathrm{sech}(r/\rho_c)(1,0,-1,0) \quad \text{if } s_1 = 1 \tag{5.10a}$$

and

$$\eta^*(r) = \sqrt{r}\ \mathrm{sech}(r/\rho_c)(0,1,0,-1) \quad \text{if } s_1 = -1. \tag{5.10b}$$

The midgap levels $\phi(r) \sim [\eta(r)/\sqrt{r}]$ have exactly the same form as the midgap levels of the doped, 1D, FM-core soliton. For the doped, vortex soliton, the gap states are empty and the valence-band continuum states are fully occupied. It is straightforward to verify that these occupied states are spin paired, as was the case for the charged domain wall in one dimension. As a result, the charged vortex soliton carries no net spin, and behaves as a bosonic excitation in the 2D antiferromagnet.

VI. DISCUSSION AND CONCLUSIONS

We have investigated the effect of a hole on the antiferromagnetic ground state of the 1D and 2D Hubbard models with a half-filled band, using self-consistent Hartree-Fock theory. For the 1D case, we have considered two types of domain walls (FM-core and AFM-core solitons) and showed that at half-filling such walls are unstable in the absence of anisotropy. Nevertheless, a host of discrete levels appear within the Mott-Hubbard gap in the presence of these magnetic textures. Upon doping, a hole can lower its energy by occupying the deepest available gap level, thereby stabilizing the domain wall. We found two self-consistent charged solitons. The stable doped soliton, centered at a site, has a pair of doubly degenerate midgap levels and is a mobile charged boson. The second solution is doped-soliton centered between sites. This is a charged boson for $US/t < 2$, but becomes an immobile charged fermion as $US/t > 2$. These results were recaptured using a very simple continuum approximation, which led to a self-consistent model of a doped soliton (a charged boson), with a pair of midgap levels. These solitons may be relevant to the superconductivity observed on the CuO chains of some cuprates,[20–23] such as $YBa_2Cu_3O_7$, which are known to have antiferromagnetically ordered chains at low temperatures.[24]

In the 2D case, we started from a *spin-flux* AFM mean-field ground state. Such a state appears if electrons have antiperiodic wave functions (due to a rotation by 2π of their spins) as they encircle any elementary plaquette of the lattice. The relativistic one-electron dispersion relations in the presence of the spin flux facilitated the description of magnetic textures. We showed a one-to-one correspondence between the electronic spectra of 1D and 2D magnetic textures. In particular, the analog of the 1D doped domain wall is a 2D doped meron vortex. The meron vortex has a pair of midgap levels, and is a mobile charged boson. The appearance of merons provides possible explanations for some of the anomalous features of the normal state of the cuprates. As the system is doped, bound meron-antimeron vortex pairs should appear. As the doping is increased or the temperature is raised, these vortex pairs may dissociate through a Kosterlitz-Thouless unbinding transition. Although this destroys the magnetic long-range order, short range spin correlations remain very strong. The non-Fermi-liquid behavior is a consequence of the fact that the charge is transported by bosons, while the midinfrared band in the optical absorption spectrum may be accounted for by absorption on the midgap levels. In the doping region relevant to high-T_c superconductivity, the quantum liquid of merons gives rise to a midgap impurity band of significant bandwidth. As the doping concentration increases further, the staggered magnetization decreases (due to the suppression in the core of the meron), the Mott-Hubbard gap closes, and normal liquid-Fermi behavior appears.

At low temperatures, merons may also combine to form charged stripes. In Fig. 15(a) we show a pair of merons with winding numbers $+1$ and -1. In Fig. 15(b) we show several merons starting to create the ''backbone'' of a horizontal charged stripe. By ''squeezing'' each other, the merons lower their energy, and form AFM domains. Domain wall solitons in 2D (charged stripes) have been the subject of intense study,[16] and it was predicted that their lowest-energy configuration corresponds to ''empty walls,'' in which all midgap states are empty. In a recent paper,[34] it was argued that populated walls should be favorable in the strong interaction limit. This type of wall has a fraction of the midgap states occupied, and therefore contributes to electrical conduction. Also, it is easy to construct hole rich and hole depleted regions.[18] A particularly striking configuration consisting of a crystalline lattice of merons is depicted in Fig. 15(c), for a doping concentration $\delta = 1/8$ per site. For this doping, it has been observed that superconductivity is suppressed.[35] Neutron scattering for $\delta = 1/8$ also reveals a magnetic superstructure in which the charge carriers are localized.[17] The stability of various configurations depends on temperatures, hole concentration, and US/t.

It is useful to extend our theory to describe the ordered and (quantum) liquid phases of merons in the doping regime pertinent to high-T_c superconductivity. This may provide a microscopic basis for the observed non-Fermi-liquid properties of the normal state of the doped Mott insulator.

ACKNOWLEDGMENTS

This work was supported in part by the Natural Sciences and Engineering Research Council of Canada, and a grant from William F. McLean. M.B. acknowledges support from the Ontario Graduate Scholarship Program.

APPENDIX A: GREEN'S FUNCTIONS IN THE MEAN-FIELD AFM BACKGROUND STATE

The Hamiltonian describing the mean-field AFM background is given by Eq. (2.1). It is useful to introduce the spinor fields $\chi_i^\dagger = (\hat{a}_{i\uparrow}^\dagger \hat{a}_{i\downarrow}^\dagger)$ and the Bloch operators $\chi_k^{(i)} = N^{-1/2}\Sigma_x \exp(-ikx_i)\chi_x^{(i)}$. Here $x_i = 2na + (i-1)a$ is the position of the site $i = 1,2$ of the nth unit cell. The sum is performed over all the N unit cells. Using the four-component operators $\Phi_k^\dagger = (\chi_k^{(1)\dagger} \chi_k^{(2)\dagger})$, the electronic part of

the mean-field Hamiltonian can be expressed as

$$\mathcal{H}_{\rm el}=\sum_k \Phi_k^\dagger \begin{pmatrix} US\sigma_z & \epsilon_k \\ \epsilon_k & -US\sigma_z \end{pmatrix} \Phi_k .$$

The sum is performed over the first Brillouin zone $-\pi/2a<k\leqslant\pi/2a$ and $\epsilon_k=-2t\cos(ka)$.

We introduce the conduction- and valence-band operators $(\chi_k^{c+},\chi_k^{v+})=\Phi_k^\dagger U$, where

$$U=\begin{pmatrix} 0 & -\alpha_k^{(-)} & 0 & \alpha_k^{(+)} \\ \alpha_k^{(+)} & 0 & -\alpha_k^{(-)} & 0 \\ 0 & \alpha_k^{(+)} & 0 & \alpha_k^{(-)} \\ -\alpha_k^{(-)} & 0 & -\alpha_k^{(+)} & 0 \end{pmatrix},$$

$\alpha_k^{(\pm)}=\sqrt{\frac{1}{2}(1\mp US/E_k)}$, and $E_k=\sqrt{\epsilon_k^2+(US)^2}$. The Hamiltonian can be expressed as

$$\mathcal{H}_{\rm el}=\sum_k E_k(\chi_k^{c+}\chi_k^c-\chi_k^{v+}\chi_k^v).$$

Therefore, the conduction band has doubly degenerate levels described by the dispersion relation $E_k^c=E_k$ while the valence band has doubly degenerate levels described by $E_k^v=-E_k$. The bands are separated by the Mott-Hubbard gap of magnitude $2US$ opened at the Fermi points $(k_o=\pm\pi/2a)$. Finally, the one-electron band wave functions are given by

$$\mathcal{C}_{k\sigma'}(m,\sigma)=\langle m\sigma|c_{k\sigma'}^\dagger|0\rangle = \frac{\delta_{\sigma,\sigma'}e^{ikma}}{\sqrt{N}}(\alpha_k^{(\sigma e_m)}e_m+\alpha_k^{(\sigma o_m)}o_m),$$

$$\mathcal{V}_{k\sigma'}(m,\sigma)=\langle m\sigma|v_{k\sigma'}^\dagger|0\rangle = \frac{\delta_{\sigma,\sigma'}e^{ikma}}{\sqrt{N}}(\alpha_k^{(-\sigma e_m)}e_m-\alpha_k^{(-\sigma o_m)}o_m).$$

Here $e_m=1$ if m is an even number and 0 if m is an odd number, and $o_m=1-e_m$.

1. Green's function

The matrix elements of the Green's function in the site-basis space are given by

$$G_{\sigma\sigma'}^0(m,n;E)\equiv\langle m\sigma|\hat{G}^0(E)|n\sigma'\rangle=\delta_{\sigma,\sigma'} \times\sum_k\left[\frac{\mathcal{C}_{k\sigma}(m,\sigma)\mathcal{C}_{k\sigma}^*(n,\sigma)}{E-E_k-i\eta} + \frac{\mathcal{V}_{k\sigma}(m,\sigma)\mathcal{V}_{k\sigma}^*(n,\sigma)}{E+E_k-i\eta}\right].$$

Substituting the band wave functions and performing the sum over the Brillouin zone, we obtain the following expressions for the Green's functions of the chain in the ground state.

(a) If m and n are both even or both odd, then

$$G_{\sigma\sigma}^0(m,n;E) =[E+(-1)^n\sigma US] \times\begin{cases} -i^{|m-n|}e^{-|m-n|\phi}(2t^2\sinh 2\phi)^{-1} & \text{if } |E|\leqslant US \\ ie^{i|m-n|\phi}(2t^2\sin 2\phi)^{-1} & \text{if } US\leqslant|E|\leqslant\gamma \\ e^{-|m-n|\phi}(2t^2\sinh 2\phi)^{-1} & \text{if } \gamma\leqslant|E|. \end{cases}$$

(b) If m and n have different parities, then

$$G_{\sigma\sigma}^0(m,n;E) =\begin{cases} i^{|m-n|-1}e^{-|m-n|\phi}(2t\cosh\phi)^{-1} & \text{if } |E|\leqslant US \\ -ie^{i|m-n|\phi}(2t\sin\phi)^{-1} & \text{if } US\leqslant|E|\leqslant\gamma \\ -e^{-|m-n|\phi}(2t\sinh\phi)^{-1} & \text{if } \gamma\leqslant|E|. \end{cases}$$

The angle $\phi>0$ is defined by

$$\phi=\begin{cases} \sinh^{-1}(\sqrt{(US)^2-E^2}/2t) & \text{if } |E|\leqslant US \\ \sin^{-1}(\sqrt{\gamma^2-E^2}/2t) & \text{if } US\leqslant|E|\leqslant\gamma \\ \sinh^{-1}(\sqrt{E^2-\gamma^2}/2t) & \text{if } \gamma\leqslant|E| \end{cases}$$

and $\gamma=\sqrt{4t^2+(US)^2}$.

APPENDIX B: GREEN'S FUNCTION OF THE SHARP-BOUNDARY SOLITON

In order to obtain a sharp-boundary soliton we must cut the chain, flip all the spins of one of the halves, and then paste the two halves back together. We calculate, below, the Green's functions at each stage.

1. Green's functions for a semi-infinite chain

Let $\mathcal{H}_{\rm el}$ be the Hamiltonian for the mean-field AFM background state, and $G_{\sigma\sigma'}^0(n,m;E)$ the corresponding Green's function. In order to find the Hamiltonian for half of this chain, we cut this chain between sites -1 and 0. Assuming that the two halves of the chain do not interact, the Hamiltonian for the chain with the cut is[36,37] $\mathcal{H}_{\rm el}^h=\mathcal{H}_{\rm el}+V_h$, where the potential V_h describing the cut is chosen such that

$$\langle n\sigma|\mathcal{H}_{\rm el}^h|n'\sigma'\rangle=0$$

if n, n' are on different sides of the cut, and

$$\langle n\sigma|\mathcal{H}_{\rm el}^h|n'\sigma'\rangle=\langle n\sigma|\mathcal{H}_{\rm el}|n'\sigma'\rangle$$

if n, n' are on the same side of the cut.

The required V_h is given by

$$\langle n\sigma|V_h|n'\sigma'\rangle=-\langle n\sigma|\mathcal{H}_{\rm el}|n'\sigma'\rangle$$

if n,n' are on different sides of the cut and vanishes otherwise.

Since $\mathcal{H}_{\rm el}$ is diagonal in the spin space, all the other operators are diagonal in the spin space. Therefore, Dyson's equation for the chain with the cut is

$$G^h_{\sigma\sigma}(n,m;E)=G^0_{\sigma\sigma}(n,m;E)+\sum_{n',m'} G^0_{\sigma\sigma}(n,n';E) \times\langle n'\sigma|V_h|m'\sigma\rangle G^h_{\sigma\sigma}(m',m;E).$$

Suppose that we first calculate the Green's function for the right-hand side of the chain, $n,m,m'\geqslant 0$. In this case, the only nonvanishing term in the sum corresponds to $n'=-1$, $m'=0$ and $\langle -1\sigma|V_h|0\sigma\rangle=t$. Then, Dyson's equation can be solved and we find the Green's function for the right-hand side of the chain:

$$G^{hR}_{\sigma\sigma}(n,m;E)=G^0_{\sigma\sigma}(n,m;E) +t\frac{G^0_{\sigma\sigma}(n,-1;E)G^0_{\sigma\sigma}(0,m;E)}{1-tG^0_{\sigma\sigma}(0,-1;E)},$$

where $n\geqslant 0$, $m\geqslant 0$.

The Green's function for the left-hand side of the chain is calculated in the same way. We also flip the spins of this half, which means changing $US\rightarrow -US$ in all expressions. We will denote by $\tilde{G}^0_{\sigma\sigma}(n,m;E)$ the Green's function obtained as a result of this substitution. Then, the Green's function for the left-hand side of the chain is given by

$$G^{hL}_{\sigma\sigma}(n,m;E)=\tilde{G}^0_{\sigma\sigma}(n,m;E)+t\frac{\tilde{G}^0_{\sigma\sigma}(n,0;E)\tilde{G}^0_{\sigma\sigma}(-1,m;E)}{1-t\tilde{G}^0_{\sigma\sigma}(-1,0;E)}$$

where $n<0$, $m<0$.

Thus, we can define the Green's function for the two disconnected halves of the chain:

$$G^h_{\sigma\sigma}(n,m;E)=\begin{cases} G^{hR}_{\sigma\sigma}(n,m;E) & \text{if } n\geqslant 0,\ m\geqslant 0\\ G^{hL}_{\sigma\sigma}(n,m;E) & \text{if } n<0,\ m<0\\ 0 & \text{otherwise.}\end{cases}$$

2. Green's function for the sharp-boundary chain

In order to obtain the Green's function for the sharp-boundary chain, we have to reconnect the two halves of the chain by subtracting the potential V_h added previously.

Dyson's equation for the Green's function of the sharp-boundary soliton is

$$G^s_{\sigma\sigma}(n,m;E)=G^h_{\sigma\sigma}(n,m;E)-tG^h_{\sigma\sigma}(n,0;E)G^s_{\sigma\sigma}(-1,m;E) -tG^h_{\sigma\sigma}(n,-1;E)G^s_{\sigma\sigma}(0,m;E).$$

This equation can be solved exactly and one obtains the following results.

(a) If $n,m\geqslant 0$, then,

$$G^s_{\sigma\sigma}(n,m;E) =G^{hR}_{\sigma\sigma}(n,m;E) +t^2\frac{G^{hR}_{\sigma\sigma}(n,0;E)G^{hL}_{\sigma\sigma}(-1,-1;E)G^{hR}_{\sigma\sigma}(0,m;E)}{F_\sigma(E)}.$$

(b) If $n\geqslant 0$, $m<0$, then,

$$G^s_{\sigma\sigma}(n,m;E)=-t\frac{G^{hR}_{\sigma\sigma}(n,0;E)G^{hL}_{\sigma\sigma}(-1,m;E)}{F_\sigma(E)}.$$

(c) If $n<0$, $m\geqslant 0$, then,

$$G^s_{\sigma\sigma}(n,m;E)=-t\frac{G^{hL}_{\sigma\sigma}(n,-1;E)G^{hR}_{\sigma\sigma}(0,m;E)}{F_\sigma(E)}.$$

(d) If $n,m<0$, then,

$$G^s_{\sigma\sigma}(n,m;E) =G^{hL}_{\sigma\sigma}(n,m;E) +t^2\frac{G^{hL}_{\sigma\sigma}(n,-1;E)G^{hR}_{\sigma\sigma}(0,0;E)G^{hL}_{\sigma\sigma}(-1,m;E)}{F_\sigma(E)}.$$

Here,

$$F_\sigma(E)=1-t^2G^{hR}_{\sigma\sigma}(0,0;E)G^{hL}_{\sigma\sigma}(-1,-1;E).$$

3. Density of states for the sharp-boundary soliton

a. Densities of states in the gaps: $|E|\leqslant US$ and $|E|\geqslant[(US)^2+4t^2]^{1/2}$

The appearance of discrete states in the gap is related to the existence of poles in the Green's functions. From the expression of Green's functions for the sharp-boundary soliton, one can see that such poles appear at the energies E satisfying the condition $F_\sigma(E)=0$. Since this condition is spin dependent, it is apparent that the direction of the spin is well defined (and unique) on each one of these levels.

Using the above Green's functions, four discrete levels appear in the gaps. Their energies are given in Sec. II C. The spin projections for these nondegenerate levels are also indicated. Clearly, charge-conjugation symmetry is preserved. For each level of energy E and spin σ there is a level of energy $-E$ and spin $-\sigma$.

The LDOS can now be calculated by using the identities

$$\frac{1}{F_\sigma(E)}=\lim_{\eta\rightarrow 0}\frac{1}{F_\sigma(E-i\eta)} =\mathcal{P}\frac{1}{F_\sigma(E)}+i\pi\sum_{\text{roots}}\frac{\delta(E-E_0)}{|dF_\sigma(E)/dE|_{E_0}},$$

where E_0 are the simple roots of the equation $F_\sigma(E)=0$, i.e. the energies of the discrete levels.

The LDOS is proportional to the imaginary part of the Green's function. This yields the following expressions for the LDOS.

In the internal gap $|E|\leqslant US$,

$$\rho^s_{n\sigma}(E)=\frac{1}{2\sqrt{1+\lambda^{-2}}}[\sqrt{\lambda^2+1}-\lambda]^{N(n)}[\delta_{\sigma,\uparrow}\delta(E-E^+_\uparrow) +\delta_{\sigma,\downarrow}\delta(E-E^-_\downarrow)].$$

In the external gaps $|E|\geqslant\sqrt{(US)^2+4t^2}$,

$$\rho^s_{n\sigma}(E)=\frac{1}{2\sqrt{1+\lambda^{-2}}}[\sqrt{\lambda^2+1}-\lambda]^{N(n)}[\delta_{\sigma,\uparrow}\delta(E-\tilde{E}^+_\uparrow)+\delta_{\sigma,\downarrow}\delta(E-\tilde{E}^-_\downarrow)].$$

Here, $\lambda\equiv US/t$ and

$$N(n)=N(-n-1)=\begin{cases} n & \text{if } n\geq 0 \text{ is even} \\ n+1 & \text{if } n\geq 0 \text{ is odd.}\end{cases}$$

b. Densities of states in the bands: $US\leq|E|\leq[(US)^2+4t^2]^{1/2}$

The diagonal matrix elements of the Green's function for the sharp-boundary chain are given by

$$G^s_{\sigma\sigma}(n,n;E)=\frac{i(E+\sigma US)}{2t^2\sin 2\phi}-e^{2i(n+1)\phi}\frac{E+\sigma US}{2t^2\sin 2\phi}\times\left[i+\frac{(E+\sigma US)}{(\sigma US\cot\phi+iE)}\right]$$

if n is even, and

$$G^s_{\sigma\sigma}(n,n;E)=\frac{i(E-\sigma US)}{2t^2\sin 2\phi}-e^{2i(n+1)\phi}\left[\frac{i(E-\sigma US)}{2t^2\sin 2\phi}+\frac{\sqrt{E^2-(US)^2}}{2t(\sigma US\cos\phi+iE\sin\phi)}\right]$$

if n is odd.

In both equations, the first term in the right-hand side represents the Green's function in the fundamental state $G^0_{\sigma\sigma}(n,n;E)$. The LDOS are now simply obtained from the definition

$$\rho^S_{n\sigma}(E)=\frac{\mathrm{sgn}(E)}{\pi}\mathrm{Im}\ G^S_{\sigma\sigma}(n,n;E).$$

[1] J. G. Bednorz and K. A. Muller, Z. Phys. B **64**, 189 (1986).

[2] See, for instance, D. M. Ginzburg, *Physical Properties of High Temperature Superconductors* (World Scientific Press, Singapore, 1992), Vols. I–V.

[3] P. W. Anderson, in *Frontiers and Borderlines in Physics* (CIV, Corso, 1988).

[4] C. M. Varma, P. B. Littlewood, S. Schmitt-Rink, E. Abrahams, and A. E. Ruckenstein, Phys. Rev. Lett. **63**, 1996 (1989).

[5] P. W. Anderson, Phys. Rev. Lett. **64**, 1839 (1990).

[6] P. W. Anderson and J. R. Schrieffer, Phys. Today **44**, 55 (1991); P. W. Anderson, Science **235**, 1196 (1987).

[7] S. Chakravarty, B. I. Halperin, and D. R. Nelson, Phys. Rev. Lett. **60**, 1057 (1988).

[8] H. Alloul, in *High Temperature Superconductivity*, edited by D. P. Tunstall and W. Barford, Proceedings of the 39th Scottish Universities Summer School in Physics, St. Andrews (Adam Hilger, New York, 1991).

[9] K. Kamagai, I. Watanabe, H. Aoki, Y. Nakamura, T. Kimura, Y. Nakamichi, and H. Nakajima, Physica B **148**, 480 (1987); J. I. Budnick, B. Chamberland, D. P. Yang, Ch. Niedermayer, A. Golnik, E. Recknagel, M. Rossmanith, and A. Weidinger, Europhys. Lett. **5**, 651 (1988); T. Thio, T. R. Thurston, N. W. Preyer, P. J. Picone, M. A. Kastner, H. P. Jenssen, D. R. Gabble, C. Y. Chen, R. J. Birgeneau, and A. Aharony, Phys. Rev. B **38**, 905 (1988).

[10] J. Kosterlitz and D. Thouless, J. Phys. C **6**, 1181 (1973); **7**, 1046 (1974).

[11] D. B. Tanner and T. Timusk, in *Physical Properties of High Temperature Superconductors III*, edited by Donald M. Ginsberg, Physical Properties of High Temperature Superconductors III (World Scientific Press, Singapore, 1992); G. A. Thomas, in Ref. 8.

[12] M. Tanaka, A. Watanabe, and J. Tanaka, Bull. Chem. Soc. Jpn. **53**, 645, 3430 (1980); A. Feldblum, J. H. Kaufman, S. Etemad, A. J. Heeger, T.-C. Chung, and A. G. MacDiarmid, Phys. Rev. B **26**, 815 (1982); T.-C. Chung, F. Moraes, J. D. Flood, and A. J. Hegger, *ibid.* **29**, 2341 (1984).

[13] S. John and A. Golubentsev, Phys. Rev. Lett. **71**, 3343 (1993); Phys. Rev. B **51**, 381 (1995).

[14] S. John and A. Müller-Groeling, Phys. Rev. B **51**, 12 989 (1995).

[15] S. John, M. Berciu, and A. Golubentsev, Europhys. Lett. **41**, 31 (1998).

[16] D. Poilblanc and T. M. Rice, Phys. Rev. B **39**, 9749 (1989); H. J. Schultz, J. Phys. (Paris) **50**, 2833 (1989); J. Zaanen and O. Gunnarsson, Phys. Rev. B **40**, 7391 (1989); J. Zaanen, M. L. Horbach, and W. van Saarloos, *ibid.* **53**, 8671 (1996).

[17] J. M. Tranquada, B. J. Sternlieb, J. D. Axe, Y. Nakamura, and S. Uchida, Nature (London) **375**, 561 (1995).

[18] V. J. Emery and S. A. Kivelson, Physica (Amsterdam) **209C**, 597 (1993); **235C-240C**, 189 (1994); in *Proceedings of the Los Alamos Symposium on Strongly Correlated Electronic Materials, 1993*, edited by K. S. Bedell (Addison-Wesley, Reading, Massachusetts, 1994).

[19] M. Steiner, J. Villain, and C. Windsor, Adv. Phys. **25**, 87 (1976).

[20] T. A. Friedmann, M. W. Rabin, J. Giapintzakis, J. P. Rice, and D. M. Ginsberg, Phys. Rev. B **42**, 6217 (1990); R. Gagnon, C. Lupien, and L. Taillefer, *ibid.* **50**, 3458 (1994).

[21] D. N. Basov, R. Liang, D. A. Bonn, W. N. Hardy, B. Dabrowski, M. Quijada, D. B. Tanner, J. P. Rice, D. M. Ginsberg, and T. Timusk, Phys. Rev. Lett. **74**, 598 (1995).

[22] K. Zhang, D. A. Bonn, S. Kamal, R. Liang, D. J. Baar, W. N. Hardy, D. Basov, and T. Timusk, Phys. Rev. Lett. **73**, 2484 (1994).

[23] J. L. Tallon, C. Bernhard, U. Binninger, A. Hofer, G. V. M. Williams, E. J. Ansaldo, J. I. Budnick, and Ch. Niedermayer, Phys. Rev. Lett. **74**, 1008 (1995).

[24] J. W. Lynn, W.-H. Li, H. A. Mook, B. C. Sales, and Z. Fisk, Phys. Rev. Lett. **60**, 2781 (1988); J. W. Lynn and W.-H. Li. J. Appl. Phys. **64**, 6065 (1988).

[25] S. Coleman, *Aspects of Symmetry* (Cambridge University, Cambridge, 1995).

[26] C. Callan, R. Dashen, and D. Gross, Phys. Lett. **66B**, 375 (1977).

[27] H. Takayama, Y. R. Lin-Liu, and K. Maki, Phys. Rev. B **21**, 2388 (1980).

[28] D. J. Gross, Nucl. Phys. B **132**, 439 (1978).
[29] E. H. Lieb and F. Y. Wu, Phys. Rev. Lett. **20**, 1445 (1968).
[30] P. W. Anderson, Phys. Rev. **115**, 2 (1959).
[31] L. Hulthen, Ark. Mat., Astron. Fys. **26A**, 11 (1938).
[32] N. W. Aschroft and N. D. Mermin, *Solid State Physics* (Saunders College Publishing, 1976), Chap. 23.
[33] T. L. Einstein and J. R. Schrieffer, Phys. Rev. B **7**, 3629 (1973).
[34] C. Nayak and F. Wilczek, Phys. Rev. Lett. **78**, 2465 (1997).
[35] A. R. Moodenbaugh, Y. Xu, M. Suenaga, T. J. Folkerts, and R. N. Shelzen, Phys. Rev. B **38**, 4596 (1988).
[36] D. Kalkstein and P. Soven, Surf. Sci. **26**, 85 (1971).
[37] E.-N. Foo and L. G. Johnson, Surf. Sci. **55**, 189 (1976).